



NASA CR-165,402

NASA Contractor Report 165402

NASA-CR-165402

1981 0022797

**MICROSTRUCTURE AND MECHANICAL PROPERTIES
OF BULK YTTRIA-PARTIALLY-STABILIZED ZIRCONIA**

Peter G. Valentine, Ralph D. Maier, and Terence E. Mitchell
Case Western Reserve University
Cleveland, Ohio

August 1981

LIBRARY COPY

OCT 5 1981

LANGLEY RESEARCH CENTER
LIBRARY, NASA
HAMPTON, VIRGINIA

Prepared for
NATIONAL AERONAUTICS AND SPACE ADMINISTRATION
Lewis Research Center
Under Grant NSG-3252



MICROSTRUCTURE AND MECHANICAL PROPERTIES
OF BULK YTTRIA-PARTIALLY-STABILIZED ZIRCONIA

Peter G. Valentine, Ralph D. Maier and Terence E. Mitchell

SUMMARY

A commercially available bulk 4.5 mole-% yttria-(Y₂O₃)-partially stabilized zirconia (PSZ) was studied with light microscopy, transmission electron microscopy, X-ray analysis, microhardness testing, and fracture toughness testing. In the as-received condition this material exhibited 34 μm equiaxed grains which were comprised of 0.05 μm coherent tetragonal precipitates situated in a cross-hatch or tweed configuration in a cubic matrix. In addition, the PSZ contained larger spheroidal and grain boundary precipitates up to 4 μm in size which were either metastable tetragonal or monoclinic in structure. Spheroids up to 2.07 μm in diameter were tetragonal; larger spheroids were monoclinic. These metastable tetragonal precipitates are the largest thus far reported for a PSZ system.

Solution annealing and air quenching the as-received PSZ eliminated the large precipitates, but fine tetragonal precipitates (0.02 μm) arranged in a cross-hatch pattern reformed during the air quench.

Both the as-received specimens and the solution-annealed-and-quenched specimens were aged at 1500°C for various lengths of time. The two aging studies yielded similar results, in that initially both had homogeneously distributed tetragonal precipitates which grew and then grouped together into particles comprised of alternating tetragonal variants. The as-received-and aged specimens reached certain points in the microstructural evolution earlier than the solution-annealed-and-quenched—and-aged specimens due to the differences in the starting points. The composition of the large spheroidal precipitates was found to be 0.9 mole-% Y₂O₃-ZrO₂.

that of the fine tetragonal precipitates was found to be 3.3 mole-% $\text{Y}_2\text{O}_3\text{-ZrO}_2$, and that of the cubic matrix was found to be 4.8 mole-% $\text{Y}_2\text{O}_3\text{-ZrO}_2$. For short agings the as-received PSZ exhibited a typical hardening behavior showing a maximum hardness of about 1400 Kg/mm^2 after 50 minutes at 1500°C . At long agings, however, the hardness again increased. The solution-annealed-and-quenched PSZ exhibited a much more sluggish hardening behavior than the as-received PSZ and it reached a maximum hardness of 1517 kg/mm^2 after 250 minutes at 1500°C . Two dimensions of the tetragonal precipitates were measured for each aging treatment. Both studies yielded similar results, with the growth of the smaller dimension following a non-linear relationship that showed a high rate of growth.

The tetragonal precipitates, which were found to have a $\{110\}$ habit plane, are in the shape of rectangular plates. The edges of the plates are along two $\langle 110 \rangle$ and one $\langle 100 \rangle$ directions. The plates appear to be stacked up, one on top of the other, in $\langle 111 \rangle$ directions. There were found to be a total of twelve different types of tetragonal precipitates.

Grinding the $\text{Y}_2\text{O}_3\text{-PSZ}$ into a powder did not cause a significant amount of metastable tetragonal to transform to monoclinic. This fact implies that transformation toughening is not a significant mechanism in this $\text{Y}_2\text{O}_3\text{-PSZ}$. The fracture toughening was found to be relatively insensitive to the aging treatments with all changes or fluctuations in K_{IC} being within the range of 2 to $3 \text{ NM/M}^{3/2}$. These values are similar to those of other PSZ's that do not exhibit transformation toughening.

MICROSTRUCTURE AND MECHANICAL PROPERTIES OF BULK YTTRIA-PARTIALLY-STABILIZED ZIRCONIA

Peter G. Valentine, Ralph D. Maier, and Terence E. Mitchell

I. INTRODUCTION

Zirconia, which exhibits three polymorphic crystal structures between room temperature and its melting temperature (monoclinic, tetragonal, and cubic), had excellent refractory properties, but the use of bulk material has been greatly limited due to the martensitic tetragonal-to-monoclinic transformation that occurs on cooling at approximately 1100°C (1,2). This transformation has an associated three percent volume expansion that often causes cracking in the bulk material (3). Cracking during thermal cycling through the transformation range (approximately $800^{\circ} \pm 1200^{\circ}\text{C}$) can sometimes be so severe that the material actually disintegrates into powder (4). Therefore, other oxides (such as CaO , MgO , and Y_2O_3) are added to the ZrO_2 to form either fully stabilized zirconias (solid solutions with the cubic fluorite structure) or partially stabilized zirconias (cubic phase material with second phase precipitates) (2,5,6). Partially stabilized zirconias have been found to have both better thermal shock resistances and mechanical properties (such as bend strength, microhardness, and fracture toughness) than either unstabilized or fully stabilized zirconias (7,8).

Considerable work has been done on the possible use of partially stabilized zirconias as thermal barrier coatings in gas turbine engines (9-15). For thermal barrier applications, compositions of 3.5 and 4.5 mole-% Y_2O_3 -partially-stabilized zirconia have been found to perform the best in thermal cycling tests (15). In general, partially stabilized zirconias that use yttria as the stabilizing oxide have been found to perform better at elevated temperatures and during thermal cycling than partially stabilized zirconias that use calcia or magnesia as the stabilizing oxide. This is, in part, due to the fact that yttria is much less volatile than calcia or magnesia and, therefore, there is less chance of the stabilizing oxide being lost. Also,

the performance of certain compositions of yttria-zirconia (such as the one used in this study) is probably improved by the fact that the high temperature tetragonal precipitates do not transform on cooling, but remain tetragonal in structure and, therefore, the cracking caused by the volume expansion that takes place when tetragonal particles transform to monoclinic ones is eliminated.

In the present work, the effects of various heat treatments on the microstructure and mechanical properties of a 4.5 mole-% Y_2O_3 -partially-stabilized zirconia were studied. The microstructures observed were characterized using optical microscopy, transmission electron microscopy, and x-ray analysis. In addition to characterizing the microstructures of the material, the microhardness and fracture toughness of the specimens were determined as a function of the heat treatments involved.

II. EXPERIMENTAL PROCEDURES

The material used for this study was a commercially available bulk 4.5 mole-percent Y_2O_3 -PSZ*. The major impurities in the zirconia are as follows: Si, Hf, Ti, and Fe.

All of the samples used were cylinders 5 mm high and 13 mm in diameter with a thickness of 1.5mm. The Y_2O_3 -PSZ was characterized in the as-received condition as well as after thermal treatments. Three types of thermal treatments were employed:

- (1) as-received material was solution annealed in the cubic solid solution region of the phase diagram, shown in Fig. 1. and then quenched in air to room temperature at a rate of over $100^{\circ}C$ per minute,
- (2) as-received material was aged in air at $1500^{\circ}C$ for various times, ranging from 25 minutes to 30 days,
- (3) solution-annealed-and-quenched material was aged in air at $1500^{\circ}C$ for various times, ranging from 25 minutes to 30 days.

*The Y_2O_3 -PSZ was produced by the Zircoa Corporation and was designated #1372.

Characterization was accomplished by standard techniques including light microscopy (LM), transmission electron microscopy (TEM), X-ray analysis, and microhardness and fracture toughness testing. In order to take optical photomicrographs and perform microhardness and fracture toughness measurements the specimens were ground with SiC paper and polished with Syton polishing liquid**. For the optical photomicrographs the samples were also thermally etched at 1500°C for 25 minutes so that grain boundaries and all other interfaces would show up more clearly. Microhardness testing was performed with a Knoop indenter at loads of 0.2 kg, while fracture toughness readings were taken with a Vickers indenter at loads of 1.0 kg (17). X-ray analysis of the phases present in both bulk and powder samples was accomplished with a diffractometer using Cu K α radiation. Electron transparent foils were prepared for TEM by grinding, polishing and ion thinning the specimens.

III. RESULTS AND DISCUSSION

Characterization of the As-Received Material

The microstructure of the as-received material, as revealed by LM, is comprised of 34 μm grains which contain a small percentage of spheroidal precipitates a few microns in size, grain boundary precipitates, and some porosity as shown in Fig. 2. The bulk density of the material was found to be 5.73 gm/cm³. This was determined according to an ASTM standard test method (designation: c 373-72 (Reapproval 1977)) The theoretical density is approximately 6.0 gm/cm³ (18), which means that the material is approximately 95.5 percent dense or has 4.5 percent porosity. TEM techniques revealed that the material consisted primarily of very fine coherent tetragonal precipitates in a cubic matrix. Bright-field TEM imaging showed only the strain contrast caused by coherent precipitates (Fig. 3a); dark-field imaging using a tetragonal {112} reflection, however, revealed tetragonal precipitates arranged in a cross-hatch or tweed-like pattern (Fig. 3b). The two visible dimensions of the particles, the width and

**Syton HT-50, a colloidal silica produced by Monsanto.

length, were found to be $0.02\text{ }\mu\text{m}$ by $0.05\text{ }\mu\text{m}$ at this orientation, which is near a $[\bar{1}11]$ zone. The microhardness of the as-received material was measured to be 1302 kg/mm^2 and the fracture toughness was found to be $2.3\text{ MN/m}^{3/2}$.

TEM was also used to demonstrate that the spheroids and grain boundary precipitates were either metastable tetragonal or monoclinic in structure. The spheroidal particles ranged in size from $0.7\text{ }\mu\text{m}$ to $3.5\text{ }\mu\text{m}$, and the grain boundary precipitates were as large as 3 to 4 μm in length. The structures of the spheroids appeared to be related to their size. Smaller spheroids were tetragonal; larger spheroids were monoclinic. Tetragonal spheroids as large as $2.1\text{ }\mu\text{m}$ were observed and appeared relatively featureless. Fig. 4 shows such a tetragonal spheroid that is $1.4\text{ }\mu\text{m}$ in diameter. Spheroidal precipitates larger than $2.1\text{ }\mu\text{m}$ exhibited a monoclinic structure and the numerous twins which are associated with the tetragonal-to-monoclinic phase transformation. The spheroid shown in Fig. 4 is shown again in Fig. 5 with the particle tilted to a $[\bar{1}11]$ zone. In this figure the outline, or boundary, of the particle is more clearly defined. The diffraction pattern, which was taken only from the precipitate, shows the reflections expected for a single tetragonal particle. Note the $\{220\}$ lattice reflections, which occur for both cubic and tetragonal phases, and the $\{211\}$ superlattice and $\{110\}$ double diffraction reflections, which occur only for the tetragonal phase. Some of the tetragonal particles observed in the electron microscope transformed from tetragonal to monoclinic while in the microscope due to the interaction of the electron beam with the particle, which probably takes place as localized heating of the specimen giving rise to stresses in the material high enough to induce the tetragonal-to-monoclinic transformation. The spheroid shown in Figs. 4 and 5 is one of the particles that were observed to transform while in the microscope. Fig. 6 shows this particle after the transformation. Note the twins associated with the monoclinic phase which lie along a $\langle 112 \rangle$ direction and normal to a $\langle 110 \rangle$ direction. Particles smaller than the $1.4\text{ }\mu\text{m}$ particle described above did not undergo the tetragonal-to-monoclinic

transformation, even when the electron beam was increased significantly in intensity and held on the particle for times as long as 30 minutes. Therefore, there seems to be some critical spheroidal particle size below which the transformation will not occur. It is noted that similar twinned spheroidal precipitates that also have undergone a martensitic transformation were reported for a Cu-1 weight-percent Fe alloy (19). A monoclinic grain boundary precipitate and the adjacent grains are shown in Fig. 7. The grains exhibit strain contrast and the precipitate has several twins running through it. Its diffraction pattern, which is similar to that shown in Fig. 6b, has the streaking associated with fine twins.

The microstructure of the commercially produced Y_2O_3 -PSZ can be explained with the aid of the Y_2O_3 - ZrO_2 phase diagram presented in Fig. 1. The microstructure suggests that the sintering operation was performed in the tetragonal + cubic two phase field at a temperature not far below the single phase cubic region. At this temperature cubic and a small percentage of tetragonal were in equilibrium. This temperature favored the formation of a few relatively large tetragonal precipitates which nucleated at energetically favorable sites, such as grain boundaries. On cooling through the two phase field, the equilibrium amount of tetragonal phase increased and numerous small coherent tetragonal particles were precipitated within the grains in a tweed configuration. On further cooling to room temperature some of the large tetragonal precipitates which had formed at the elevated sintering temperature transformed to equilibrium monoclinic and experienced considerable twinning. Spheroids 2.1 μm or less in diameter did not undergo this transformation and remained as metastable tetragonal. It is noted that these spheroids are larger than any metastable tetragonal particles previously reported for PSZ systems (18, 20, 21). In particular, Gupta (21) working with a PSZ containing small amounts of Y_2O_3 found that metastable tetragonal grains could be retained at room temperature if the grain size was below 0.3 μm .

Characterization of the Solution-Annealed-and-Quenched Material

A solution annealing treatment significantly modified the microstructure of the PSZ. The material was annealed in the single phase cubic region shown in Fig. 1 and then air quenched to room temperature. The annealing treatment dissolved all of the second phase precipitates. LM revealed the absence of the large spheroidal and grain boundary precipitates evident in the as-received material (Fig. 8). In addition, grain growth at the annealing temperature caused the grain size to increase from 34 to 42 μm . Bright-field TEM revealed only strain contrast (Fig. 9a) similar to that observed for the as-received PSZ (Fig. 3a). In dark-field, coherent tetragonal particles, which precipitated in the cubic matrix during the air quench to room temperature, were observed, as shown in Fig. 9b. The two visible dimensions of these particles were found to be 0.01 μm by 0.02 μm at this orientation, which is near a $[\bar{1}11]$ zone. The microhardness of this material was measured to be 1376 kg/mm^2 and the fracture toughness was found to be 2.3 $\text{MN/m}^{3/2}$. The high hardness is attributed to the presence of the coherent tetragonal precipitates.

Influence of Aging on the Microstructure and Microhardness of the As-Received Material

The influence of aging on the microstructure and microhardness of the as-received PSZ was also studied. The microhardness is presented as a function of aging time at 1500°C in Fig. 10. The PSZ initially exhibits a typical precipitation hardening behavior, attaining a peak hardness of 1397 kg/mm^2 , but at the longer aging times, 4,515 and 10,080 minutes, the hardness again rises to approximately 1365 kg/mm^2 . The drop in hardness after the peak value obtained at 50 minutes is probably due to an over-aging of the fine tetragonal precipitates. The rise in hardness associated with the longer agings is probably due to the transformation of the large tetragonal spheroidal and grain boundary precipitates to monoclinic. The longest aging, 43,200 minutes, had a hardness of 1444 kg/mm^2 , which

is the highest hardness obtained for all of the aged and unaged as-received PSZ specimens. This data point does not fit in well with the others, probably due to the fact that the specimen aged for 43,200 minutes was found to have a slightly different composition from the other samples.

The compositions of three of the aged and unaged as-received specimens were measured using EDAX attachments on an analytical TEM and on a scanning electron microscope (SEM). In an unaged as-received specimen compositional measurements were made in two areas, in a large spheroidal precipitate and in an area containing both cubic matrix and fine tetragonal precipitates. When measuring only the percentages of Y_2O_3 and ZrO_2 in the two areas, the large spheroidal precipitate was found to be 0.9 mole-% Y_2O_3 - ZrO_2 . This is as expected according to the phase diagram which shows that tetragonal precipitates that form at high temperatures, such as the spheroidal precipitates that formed during sintering in the two-phase region just below the solvus line, have Y_2O_3 contents significantly less than the cubic matrix. The concentrations of two of the largest impurities in the material, SiO_2 and HfO_2 , were also measured to see if there was a segregation of the impurities to specific areas. For both impurities the concentrations were found to be approximately the same in both the spheroidal precipitate and in the area containing cubic matrix and tetragonal precipitates. Only relative values could be determined for the SiO_2 content, which was measured with an SEM, but the HfO_2 content was found to be 1.4 mole-% in the spheroidal particle and

1.6 mole-% in the cubic-matrix-plus-fine-tetragonal-precipitate area. In an as-received specimen that was aged for 1,525 minutes compositional measurements of the Y_2O_3 and ZrO_2 contents were made both in the cubic matrix and in one of the small tetragonal precipitates. The small tetragonal precipitate was found to be 3.3 mole-% Y_2O_3 - ZrO_2 while the cubic matrix was found to be 4.8 mole-% Y_2O_3 - ZrO_2 . This is also as expected because the fine precipitates formed and grew at temperatures below that at which the material was sintered. At these lower temperatures the Y_2O_3 concentration increases for both the tetragonal and cubic phases. In an as-received specimen that was aged for 43,200 minutes compositional measurements were made of the Y_2O_3 and ZrO_2 contents in only one area. This area consisted of cubic matrix and very fine tetragonal precipitates, which were found to be 0.003 μm by 0.022 μm when imaged near a $[\bar{1}11]$ zone. The composition of the cubic-tetragonal area was found to be 5.7 mole-% Y_2O_3 - ZrO_2 , which is about one mole-percent higher than any of the other specimens. This slight increase in Y_2O_3 content was evidently enough to put the specimen in the single phase cubic solid solution region of the phase diagram at 1500°C because the tetragonal precipitates which had been growing with aging time for the other specimens were found to be smaller in this specimen than in any of the other specimens, including those solution-annealed at much higher temperatures and then quenched. The presence of these very fine precipitates suggest that the solvus line of the phase diagram should be moved to lower Y_2O_3 concentrations (to the left) for the region around 1500°C and 5-6 mole-% Y_2O_3 . Apparently, this specimen was in the single-phase cubic-solid-solution region at 1500°C and, when cooled to room temperature, passed through the two-phase cubic-tetragonal region, which allowed the nucleation and growth of fine tetragonal precipitates to begin.

LM revealed that aging at 1500°C increased the grain size from 34 to 61 μm in 43,200 minutes. Fig. 11 is an optical micrograph of the as-received material after aging for 43,200 minutes. Note the porosity and large numbers of grain boundary precipitates. Bright-and dark-field TEM views of the un-aged as-received specimen tilted close to a $[013]$ zone are shown in Figs. 12a and 12b. In bright-field only strain contrast is visible, but in dark-field the fine tetragonal precipitates are seen in a tweed pattern. Note that the precipitates are relatively equiaxed and are arranged uniformly throughout the matrix. Hanniak (22) has also reported a microstructure that is quite similar to that shown in Fig. 12b for a 5.1 mole-% $\text{Y}_2\text{O}_3\text{-ZrO}_2$ in the as-fired condition. With aging, the precipitates grew and the strain contrast, and therefore the strain in the material, decreased, allowing improved imaging of the tetragonal precipitates. Bright- and dark-field views of the precipitates in the material aged for 250 minutes at 1500°C are presented in Figs. 13a and 13b. These micrographs were taken with the specimen oriented near a $[013]$ zone so that changes due to the aging treatment could readily be seen by comparison with the preceeding figure, Fig. 12. Note that after 250 minutes at 1500°C the precipitates have become elongated, but are still relatively uniformly distributed throughout the matrix. After aging the as-received material for 1,525 minutes at 1500°C the precipitates were found to coalesce to form particles comprised of alternating variants. This structure, made up of precipitates grouped together to form larger particles, is shown in Fig. 14. As before, the specimen was tilted close to a $[013]$ zone so that direct comparison of the aging treatments could be made.

N82-10245 #

It was found by optical observations of cracks induced during the fracture toughness measurements and by TEM that failure (cracking) of the material usually occurred at grain boundary precipitates. A cracked grain boundary precipitate is shown in Fig. 15a. The crack can be seen running along the interface between the precipitate and the adjacent grains and through the precipitate itself. Note also that twinning has occurred along three different planes in the precipitate and that the diffraction pattern for the precipitate shows some evidence of diffraction spot streaking in three directions associated with the three twinning planes (Fig. 15b).

Influence of Aging on the Microstructure and Microhardness of the Solution-Annealed-and-Quenched Material

The solution-annealed material was also aged for various lengths of time at 1500°C to permit the influence of aging time on microstructure and mechanical behavior to be established. The microhardness is presented as a function of aging time at 1500°C in Fig. 16. The solution-annealed-and-quenched material reached a peak hardness of 1517 kg/mm² after approximately four hours at 1500°C and its hardness did not diminish significantly until after three days at 1500°C. The solution-annealed-and-quenched material was found to require a longer time at 1500°C to reach its peak hardness than the as-received material. Also, once the peak hardness was reached, much longer times than those required for the as-received material were needed in order for the hardness to drop significantly. The drop in hardness is probably due to a combination of phenomena. These are the overaging and coalescence of the tetragonal precipitates and the formation and growth of grain boundary precipitates. The aging behavior of the solution-annealed-and-quenched PSZ is much more sluggish, and yields higher hardnesses, than that of partially stabilized zirconias that contain oxides other than Y₂O₃, such as MgO. For example, in an 8.1 mole-% MgO-PSZ (1) that was aged at 1400°C, a peak hardness of 1174 kg/mm² occurred after 30 minutes and, upon further aging, the hardness dropped rapidly to approximately 800 kg/mm². LM of the solution-annealed-and-quenched material revealed that aging at 1500°C increased the grain size from 42 μm to 51 μm in 43,200 minutes. After

aging for 43,200 minutes a large number of grain boundary precipitates, which seem to be primarily (if not totally) monoclinic, have formed (Fig. 17).

The primary difference between the initial microstructures and those developed by aging at 1500°C for the two different aging studies, that of the as-received material and that of the solution-annealed-and-quenched material, are given below. The primary difference between the aging studies is that the as-received material, and therefore the aged specimens of the as-received material, has numerous spheroidal and grain boundary precipitates that are either tetragonal or monoclinic while the solution-annealed-and-quenched material, and the earlier aged specimens of the solution-annealed-and-quenched material, show no evidence of such precipitates. However, at long aging times, the solution-annealed-and quenched material does have a significant number of grain boundary precipitates. As far as the fine tetragonal precipitates are concerned, both aging studies show approximately the same microstructural development and evolution, except that the as-received specimens, when aged, reach the different stages of microstructural evolution at earlier times due to the fact that the unaged as-received specimens had larger tetragonal precipitates than did the unaged solution-annealed-and-quenched specimens. Finally, the grain size of the solution-annealed-and-quenched material is larger than that of the as-received material, 42 μm vs. 34 μm , but after aging for 43,200 minutes the solution-annealed-and-quenched material achieved a grain size of only 51 μm , while the as-received material achieved a grain size of 61 μm (note: the composition of the as-received specimen that was aged the longest was found to be slightly higher in Y_2O_3 and the fine microstructure was significantly different from the preceeding specimens in the as-received aging study).

Growth of Fine Tetragonal Precipitates Due to Aging at 1500°C

The growth of the fine tetragonal precipitates with respect to time at 1500°C was characterized by TEM. All specimens were tilted or oriented close to a $[\bar{1}11]$ zone for ease of comparison between the different specimens (other zones could have been used). With the specimens in this

orientation the fine tetragonal precipitates were found to be approximately rectangular in shape (only two dimensions visible) with one dimension usually being much less than the other except at very short aging times. Fig. 18 is a plot of the growth of the two measureable dimensions of the tetragonal precipitates with respect to time at 1500°C for the two aging studies. As can be seen, both aging studies demonstrate the same growth characteristics; the smaller dimension of the precipitates grows in a linear fashion while the larger dimension grows at a much greater rate with an ever-increasing slope (at least as far as this work is concerned). The only real difference between the growth curves for the as-received material and those for the solution-annealed-and-quenched material is that the as-received curves start at larger precipitate sizes, due to their prior thermal history, and, because the microstructural evolutions are similar, the curves for the as-received specimens are always higher than those for the solution-annealed-and-quenched specimens. As noted before, the last or longest aged specimen for the as-received aging study does not fit in properly with the other specimens.

The growth of the tetragonal precipitates for both aging studies is described below, making use of dark-field images of the precipitates from both studies at the following aging times at 1500°C : 0, 50, 250, 1,525, 10,080, and 43,200 minutes. All of the dark-field micrographs discussed below were taken of specimens tilted close to $[\bar{1}11]$ zones. In all cases the tetragonal precipitates were found to lie along $\langle 112 \rangle$ directions. The tetragonal precipitates in the unaged as-received material ($0.02\text{ }\mu\text{m}$ by $0.05\text{ }\mu\text{m}$) were distributed homogeneously throughout the cubic matrix (Fig. 3b). Aging for 50 minutes caused some precipitate growth ($0.02\text{ }\mu\text{m}$ by $0.06\text{ }\mu\text{m}$) but did little else, with the precipitates still distributed uniformly throughout the cubic matrix (Fig. 19). After 250 minutes of aging the rate of growth of the precipitates had again increased, and the precipitates ($0.03\text{ }\mu\text{m}$ by $0.13\text{ }\mu\text{m}$) had begun to show evidence of grouping together to form larger particles (Fig. 20). The rate of growth continued to increase as evidenced by the precipitates imaged after aging for 1,525 minutes. These precipitates ($0.03\text{ }\mu\text{m}$ by $0.18\text{ }\mu\text{m}$) were found to be grouped

together into particles made up of alternating tetragonal variants (see Fig. 35, below). 10,080 minutes of aging time increased the growth rate once again and caused the banded particles to increase in size and number of precipitates ($0.04\text{ }\mu\text{m}$ by $0.32\text{ }\mu\text{m}$) per banded particle (Fig. 21). The specimen aged the longest for the as-received study does not fit in with the rest properly because its composition varied significantly. This specimen was found to contain very fine tetragonal precipitates ($0.003\text{ }\mu\text{m}$ by $0.022\text{ }\mu\text{m}$) (Fig. 22a). In bright-field (Fig. 22b) this specimen showed no evidence of the tetragonal precipitates, but showed only strain contrast and bend contours. In a manner similar to that described above for the aging study of the as-received material, the rate of growth of the tetragonal precipitates increased with each successive time increment at 1500°C for the aging study of the solution-annealed-and-quenched material. In the unaged condition, the precipitates ($0.01\text{ }\mu\text{m}$ by $0.02\text{ }\mu\text{m}$) were found to be relatively equiaxed and homogeneously distributed (see Fig. 9b). After 50 minutes of aging the precipitate structure showed little change except that the precipitates ($0.02\text{ }\mu\text{m}$ by $0.04\text{ }\mu\text{m}$) were slightly larger (Fig. 23). The microstructure obtained when the solution-annealed-and-quenched material was aged for 50 minutes at 1500°C is very similar to that obtained by Hannik (22) for a solution-treated 5.1 mole-% $\text{Y}_2\text{O}_3\text{-ZrO}_2$ that was aged for 100 hours at 1300°C ; and in both cases the precipitates are shown aligned in a $\langle 112 \rangle$ direction. 250 minutes of aging time also brought about little change except for a small increase in the precipitate size ($0.02\text{ }\mu\text{m}$ by $0.08\text{ }\mu\text{m}$) (Fig. 24). Aging for 1,525 minutes caused the precipitates ($0.03\text{ }\mu\text{m}$ by $0.16\text{ }\mu\text{m}$) to begin to group together to form the larger banded particles (Fig. 25). The banded particles were found to be fully developed in the specimen aged for 10,080 minutes, with the individual precipitates ($0.03\text{ }\mu\text{m}$ by $0.24\text{ }\mu\text{m}$) becoming quite long (Fig. 26). The final aging of the solution-annealed-and-quenched material, for 43,200 minutes, caused the banded particles and the individual precipitates ($0.04\text{ }\mu\text{m}$ by $0.60\text{ }\mu\text{m}$) to increase in size substantially, yielding the largest particles and/or fine precipitates observed in either aging study (Fig. 27).

Determination of the Habit Plane of the Tetragonal Precipitates

In order to determine the habit plane(s) of the tetragonal precipitates, images of the precipitates had to be photographed at several different orientations. The orientations used for this are all close to five different zone axes, which are the [013], the [012], the [011], the $[\bar{1}11]$, and the $[\bar{1}12]$ zone axes. These axes, along with the [001] zone axis, are most of the more commonly used zone axes on the unit stereographic triangle. Fig. 28 shows the unit stereographic triangle for cubic (f.c.c.) zirconia with tetragonal precipitates. The locations of the six zones mentioned above and the diffraction patterns associated with these zones are placed on or near the triangle shown in Fig. 28. Actual diffraction patterns obtained by TEM from samples used in the two aging studies are presented in Fig. 29. Figs. 29a, 29b, 29c, 29d, and 29e are, respectively, [001], [013], [012], [011], and $[\bar{1}12]$ zones. Below each of the diffraction patterns the different diffraction spots pertaining to each zone are indexed. These zone axes are representative of those obtainable from each of the specimens used in this work.

The information needed to determine the habit plane(s) was obtained by taking dark-field micrographs of the tetragonal precipitates near each of the five zones discussed above. Fig. 30 is a dark-field micrograph of the tetragonal precipitates in the as-received specimen aged for 1,525 minutes at 1500°C that has been tilted to near a [013] zone. In this figure the precipitates can be seen to lie along two $\langle 3\bar{3}1 \rangle$ directions. All of the dark-field micrographs used for the habit plane determination were taken of the same as-received sample aged for 1,525 minutes at 1500°C. Fig. 31, which is another dark-field micrograph, shows the precipitates directed along two $\langle 2\bar{2}1 \rangle$ directions when the foil is tilted close to a [012] zone. In Fig. 32 the specimen has been oriented close to a [011] zone and, in dark-field, the precipitates can be observed running along two $\langle 1\bar{1}1 \rangle$ directions. When the foil is tilted close to a $[\bar{1}12]$ zone, the precipitates, when imaged in dark-field, lie along two $\langle 311 \rangle$ directions (Fig. 33).

A typical $[\bar{1}11]$ zone, found in either of the two aging studies, is shown in Fig. 34. In this figure, below the actual micrograph, the spot pattern is reproduced and indexed, showing $\{220\}$, $\{112\}$, and $\{110\}$ spots. The $\{220\}$ reflections are due to the cubic matrix and to the tetragonal precipitates. The $\{112\}$ reflections are superlattice spots and are due to the three possible variants of the tetragonal phase. These three variants arise from the c-axis of the tetragonal unit cell being able to line up in any one of three $\langle 100 \rangle$ cubic directions. The other reflections shown in Fig. 34 are $\{110\}$ spots, which are due to double diffraction. Using each of the three different types of $\{112\}$ spots, in this case the $(\bar{2}\bar{1}\bar{1})$, the $(\bar{1}\bar{2}\bar{1})$, and the $(\bar{1}\bar{1}\bar{2})$ spots, the three different variants of the tetragonal phase were illuminated by dark-field imaging. Figs. 35a, 35b, and 35c, which are each of the exact same area, all show a single tetragonal variant illuminated. From these micrographs it can be clearly seen, with the aid of Fig. 35d which shows the same area in bright-field and has the corresponding diffraction pattern oriented properly, that the banded particles are each made up of two tetragonal variants, with the alternating precipitates each being of the same variants. Also, note that each variant accounts for two types of precipitates that lie at angles of 60° (or 120°) to each other. Thus, a total of six types of precipitates can be illuminated when micrographs are taken of the dark-field images obtained using the three different types of $\{112\}$ spots from a particular $[111]$ zone. Note that all of these precipitates lie along $\langle 112 \rangle$ directions.

The habit plane(s) of the tetragonal precipitates was found to be a $\{110\}$ plane. Earlier work (22) has shown that the habit plane was either a $\{100\}$ or a $\{110\}$ plane, but the two possibilities could not be distinguished from each other. The habit plane was determined by considering the precipitate directions, given in Figs. 30, 31, 32, 33, and 35, as traces of lower index planes. Fig. 36 is a table of the directions that correspond to traces of specific planes in specific

zones. This figure shows all the possible traces for $\{100\}$ and $\{110\}$ planes in the five zones discussed above. Also, the specific traces determined from the dark-field micrographs given in the preceding figures are given. All of the traces obtained from the dark-field images are of $\{110\}$ planes, which indicates that the habit plane is a $\{110\}$ plane and not a $\{100\}$ plane. Note, also, that the six types of tetragonal precipitates illuminated using the three $\{112\}$ spots lie on only three of the six $\{110\}$ planes. Therefore, there must actually be twelve different types of tetragonal precipitates arranged on six planes with two types per plane. The six types of precipitates not illuminated in Fig. 35 most probably would show up by dark-field techniques with the specimen tilted to a different $[111]$ zone.

Determination of the Shape of the Tetragonal Precipitates

Now that we have determined the habit planes of the tetragonal precipitates to be $\{110\}$ planes, the shape of the tetragonal precipitates can best be determined by looking at a specimen tilted close to a $[011]$ zone. Figs. 37a and 37b show the as-received specimen aged for 1,525 minutes at 1500°C oriented close to such a zone. In these figures, where 37b is a higher magnification of approximately the same area shown in 37a, the precipitates can be seen to be roughly rectangularly shaped plates. The dark areas are precipitates that are viewed looking normal to the largest of their faces. These faces are seen to be roughly rectangular or somewhat distorted ellipses. From these dark precipitates two of the three dimensions of the plates can be determined. The other dimension, the thickness of the plates, can be determined by looking at the light banded areas in the figures. These areas are precipitate plates viewed edge on showing the two smaller dimensions of

the plates. As noted before these banded areas are made up of two variants stacked up one on top of the other. The edges of the plates are seen to lie in two $\langle 110 \rangle$ and one $\langle 100 \rangle$ directions. Also, the precipitate plates appear to be stacked up, one on top of the other, in $\langle 111 \rangle$ directions. The rectangular shape of the plates can be seen more clearly in Fig. 38. This figure shows the solution-annealed-and-quenched specimen that has been aged for 10,080 minutes and is tilted to such an orientation that the bands in the banded particles are observed running in a $\langle 311 \rangle$ direction. In this figure all three dimensions, although not exactly true dimensions, can be seen. The two smaller dimensions can be determined from the banded particles which are groups of precipitates viewed approximately edge on, and the third dimension can be determined from the other type of particle seen in the figure. These particles appear relatively featureless, similar to the matrix, with only their boundaries being visible. In all of these particles seen in the figure, the outlines of several precipitates stacked up one on top of the other can be observed. These particles, showing the outlines of several precipitates in each, show more clearly than Figs. 37a and 37b the rectangular nature of the large faces of the individual precipitates.

X-Ray Analysis of the Influence of Aging on the As-Received and Solution-Annealed-and-Quenched Materials

The structures of the aged and unaged specimens were also studied by X-ray analysis with a diffractometer using Cu K α radiation. X-ray analysis also demonstrated that the amount of strain within the material (discussed earlier) decreased with aging time at 1500°C. This reduction in strain is indicated by the fact that the diffraction peaks become narrower with increasing aging time, as shown in Fig. 39 for the as-received material. The portion of the diffractometer scans shown contains the cubic (400) and the tetragonal (400) and (004) peaks. Because the cubic and tetragonal lattice parameters are only slightly different, these peaks are difficult to separate.

When CaO- or MgO-PSZ (1, 20, 22) is ground into powder form for X-ray analysis, the metastable tetragonal precipitates retained at room temperature transform to monoclinic because of the removal of the constraint of the matrix. This transformation also occurs in the vicinity of cracks which propagate through the material and is believed to enhance the toughness of the PSZ. This toughening mechanism has been called transformation toughening. However, it has been reported that tetragonal precipitates in Y_2O_3 -PSZ do not transform to monoclinic on grinding (22). Similar results were also obtained in this study. Grinding was found to have little if any influence on the percentage of monoclinic phase. Thus, it appears that transformation toughening is not a significant mechanism in this Y_2O_3 -PSZ. The improved properties of this material are probably primarily associated with precipitation strengthening instead.

Influence of Aging on the Fracture Toughness of the As-Received and Solution-Annealed-and-Quenched Materials

The fracture toughness of the aged and unaged as-received material and of the aged and unaged solution-annealed-and-quenched material was measured using an overloaded microhardness testing machine with a Vickers indenter and a load of 1 kg. In all cases the fracture toughness was found to be between 2 and 3 $MN/m^{3/2}$ (except for the longest aging of the as-received material, which, as noted before, had a higher Y_2O_3 concentration). Fig. 40 shows the effect of aging at 1500°C on the fracture toughness of both the as-received and solution-annealed -and-quenched materials. The fracture toughness was found to be relatively insensitive to the aging treatments with all changes or fluctuations in K_{IC} , the fracture toughness, being within the range of 2 to 3 $MN/m^{3/2}$. For the as-received material a slight peak was observed in the K_{IC} values for aging times of 1,525 and 4,515 minutes, after which the fracture toughness dropped

back down. This peak in the K_{IC} curve may be associated with the formation of the banded particles made up of alternating tetragonal variants which are observed to form at these aging times. The final drop in K_{IC} is probably due to the increase in monoclinic spheroidal and grain boundary precipitates that occurs at the longer aging times. The K_{IC} curve of the solution-annealed-and quenched material shows two slight peaks, the first around 50 minutes and the second around 10,080 minutes. The only observed difference between unaged specimens and those aged for 50 minutes that might account for the first peak is the development of elongated precipitates from roughly equiaxed ones. Continued precipitate growth accompanies the subsequent drop in K_{IC} . The second peak in the K_{IC} curve, as with the peak in the K_{IC} curve for the as-received material, may be associated with the formation of the banded particles and the subsequent drop in K_{IC} , as before, is probably due to the increase in monoclinic grain boundary precipitates. The fracture toughness of the 4.5 mole-% Y_2O_3 -PSZ used in this study and those of several other PSZ's are given in Fig. 41 in tabular form. From the figure, it can be seen that the PSZ's that do not transformation toughen, which includes that of the present study, have K_{IC} 's between 1 and 3, while PSZ's that do transformation toughen have K_{IC} 's between 5 and 9.

IV CONCLUSIONS:

- 1) The commercially available 4.5 mole-% Y_2O_3 -PSZ studied contains a few large spheroidal and grain boundary precipitates up to 4 μm in size which are either metastable tetragonal or monoclinic in structure and small 0.05 μm tetragonal precipitates arranged in a tweed pattern.
- 2) Spheroidal precipitates up to 2.07 μm in diameter were metastable tetragonal; large spheroidal precipitates transformed to monoclinic.
- 3) Solution annealing and quenching the PSZ dissolved all of the precipitates, but very fine 0.02 μm tetragonal particles formed in a tweed configuration during the air quench.
- 4) For short agings the as-received PSZ exhibited a typical hardening behavior showing a maximum hardness of about 1400/Kg/mm² after 50 minutes at 1500°C. At long agings, however, the hardness again increased.
- 5) EDAX analysis showed that the large spheroidal precipitates were 0.9 mole-% Y_2O_3 -ZrO₂, the fine tetragonal precipitates were about 3.3 mole-% Y_2O_3 -ZrO₂, and the cubic matrix was approximately 4.8 mole-% Y_2O_3 -ZrO₂.
- 6) The solution-annealed-and-quenched PSZ exhibited a much more sluggish hardening behavior than the as-received PSZ and it reached a maximum hardness of 1517 Kg/mm² after 250 minutes at 1500°C.
- 7) The primary difference between the two aging studies is that the as-received material, and therefore the aged specimens of the as-received material, has numerous spheroidal and grain boundary precipitates that are either tetragonal or monoclinic while the solution-annealed-and-quenched materials and the earlier aged specimens of the solution-annealed-and-quenched material, shows no evidence of such precipitates. However, at long aging times, the solution-annealed-and-quenched material

does have a significant number of grain boundary precipitates.

- 8) As far as the fine tetragonal precipitates are concerned both aging studies show approximately the same microstructural development and evolution except that the as-received specimens, when aged, reach the different stages of microstructural evolution at earlier times due to the fact that the unaged as-received specimens had larger tetragonal precipitates than did the unaged solution-annealed-and-quenched specimens. This micro-structural development and evolution involved the formation and growth of fine homogeneously distributed tetragonal precipitates into particles comprised of alternating tetragonal variants.
- 9) The growth of the tetragonal precipitates in both aging studies was found to be similar. Two dimensions of the precipitates were measured for each aging treatment, and the growth of the smaller dimension was found to be a linear relationship while the other dimension increased at a much greater rate.
- 10) The tetragonal precipitates were found to have a {110} habit plane. there were found to be a total of twelve different orientations of tetragonal precipitates.
- 11) The tetragonal precipitates were found to be in the shape of rectangular plates, with the edges of the plates being along two $\langle 110 \rangle$ and one $\langle 100 \rangle$ directions. Also, the precipitate plates appear to be stacked up, one on top of the other, in $\langle 111 \rangle$ directions.
- 12) Grinding the Y_2O_3 -PSZ into a powder did not cause a significant amount of metastable tetragonal to transform to monoclinic. This fact implies that transformation toughening is not a significant mechanism in the Y_2O_3 -PSZ of this study.
- 13) The fracture toughness was found to be relatively insensitive to the aging treatments with all changes or fluctuations in K_{IC} being within the range of 2 to 3 $MN/m^{3/2}$. These values are similar to those of other PSZ's that do not exhibit transformation toughening.

References

1. Douglas Lloyd Porter; "Microstructure-Mechanical Property Relationships in an MgO-Partially-Stabilized Zirconia"; Ph.D. Thesis, 1977; Case Western Reserve University, Cleveland, Ohio 44106.
2. G. K. Bansal and A. H. Heuer; "Precipitation in Partially Stabilized Zirconia" Journal of The American Ceramic Society, Vol. 58, 1975, pp. 235-238.
3. R. N. Patil and E. C. Subbarao; "Axial Thermal Expansion of ZrO_2 and HfO_2 in the Range Room Temperature to $1400^\circ C$;" Journal of Applied Crystallography, Vol. 2 [Pt. 6], 1969, pp. 281-288.
4. A. C. D. Chaklader and V. T. Baker; "Reactive Hot-Pressing: Fabrication and Densification of Non-Stabilized ZrO_2 ;" American Ceramic Society Bulletin, Vo. 44 [3] 1965, pp. 258-259.
5. Eugene Tyshkewitch; Oxide Ceramics; Academic Press, Inc., New York, 1960, pp.350-396.
6. R. C. Garview; High Temperature Oxides, Part II Edited by A.M. Alper; Academic Press, Inc. New York and London, 1970, pp. 118-132.
7. R. E. Jaeger and R. E. Nickell; Ceramics in Severe Environments (Materials Science Research, Vol. 5) Edited by W. W. Kriegel and Hayne Palmont III; Plenum Press New York, 1971, pp. 163-184.
8. R. C. Garview and P. S. Nicholson; "Structure and Thermomechanical Properties of Partially Stabilized Zirconia in the $CaO-ZrO_2$ System;" Journal of the American Ceramic Society, Vol. 55 [3], 1972, pp. 152-157.
9. C. H. Liebert and F. S. Stepka; "Potential Use of Ceramic Coating as a Thermal Insulation on Cooled Turbine Hardware;" NASA TM X-3352, 1976.
10. C. H. Liebert, R. E. Jacobs, S. Stecura, and R. C. Morse, "Durability of Zirconia Thermal Barrier Ceramic Coatings on Air-Cooled Turbine Blades in Cyclic Jet Engine Operation," NASA TM X-3410.
11. S. Stecura and C. H. Liebert, "Thermal Barrier Coating System," U.S. Patent no. 4,055,705, Oct. 1977.
12. S. Stecura, "Two-Layer Thermal Barrier Coating Coating for Turbine Airfoils-Furnace and Burner Rig Test Results, "NASA TM X-3425, 1976.
13. S. Steiura, "Two-Layer Thermal Barrier Coating High Temperature Components," American Ceramic Society Bulletin, Vol. 56, 1977, pp. 1082-1085.
14. R. D. Maier, C. M. Scheuermann, and C. W. Andrews, "Characterization of the Degradation of a Two-Layer Thermal Barrier Coating System under Thermal Cycling Conditions," American Ceramic Society Bulletin.
15. S. Stecura, "Effects of Compositional Change on the Performance of a Thermal Barrier Coating System, "NASA TM 78976.

16. V. S. Stubican, R. C. Hink, and S. P. Ray, "Phase Equilibrium and Ordering in the System ZrO_2 - Y_2O_3 ," *Journal of the American Ceramic Society*, Vol. 61 [1-2], 1978, pp. 17-21.
17. A. G. Evans and E. A. Charles "Fracture Toughness Determinations by Indentation," *Journal of The American Ceramic Society*, Vol. 59, 1976, pp. 371-372.
18. P. H. Riety, J. S. Reed, and A. W. Naumann, " Fabrication and Flexural Strength of Ultrafine-Grained Yttria-Stabilized Zirconia, " *American Ceramic Society Bulletin*, Vol. 55, No. 8, pp. 713-722.
19. Masaharu Kato, Ryoichi Monzeu and T. Mori, " A Stress-Induced Martensitic Transformation of Spherical Iron Particles in a Cu-Fe Alloy, " *Acta Metallurgical* Vol. 26, 1978, pp. 605-613.
20. R. C. Garvie, R. H Hannink and R. T. Pascoe, "Ceramic Steel?" *Nature*, Vol. 258, December 25, 1975, pp. 703-704.
21. T. K. Gupta, J. H. Bechtold, R. C. Kuznicki, L. H. Cadoff and B. R. Rossing, "Stabilization of Tetragonal Phase in Polycrystalline Zirconia, " *Journal of Materials Science*, Vol. 12, 1977, pp. 2421-2426.
22. R. H. J. Hannik, "Growth Morphology of the Tetragonal Phase in Partially Stabilized Zirconia," *Journal of Materials Science* Vol. 13, 1978, pp. 2487-2496.
23. D. J. Green, P. S. Nicholson, and J. D. Embury, "Fracture Toughness of a Partially Stabilized ZrO_2 in the System CaO - ZrO_2 ," *Journal of the American Ceramic Society*, Vo. 56[12] 1973, pp 619-623.
24. T. K. Gupta, "Role of Stress-Induced Phase Transformation Enhancing Strength and Toughness of Zirconia Ceramics, " from Fracture Mechanics of Ceramics, Vol. 4, Edited by R. C. Bradt, D.P.H. Hasselman, and F. F. Lange, Plenum Publishing Corporation, 1978.

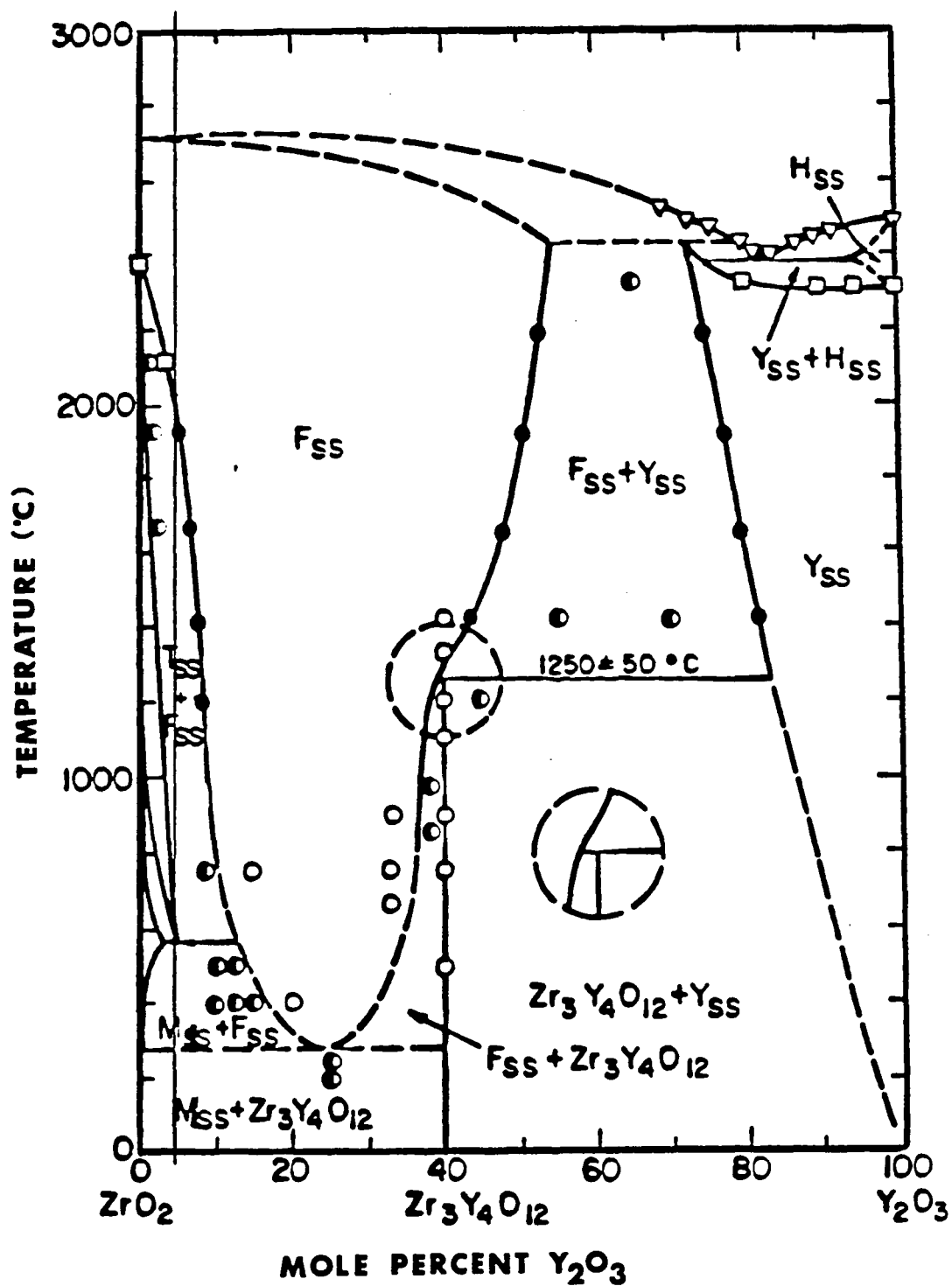


FIGURE 1: Equilibrium phase diagram for the system ZrO_2 - Y_2O_3 (16). The vertical line at the 4.5 mole-% Y_2O_3 represents the composition employed in this study.

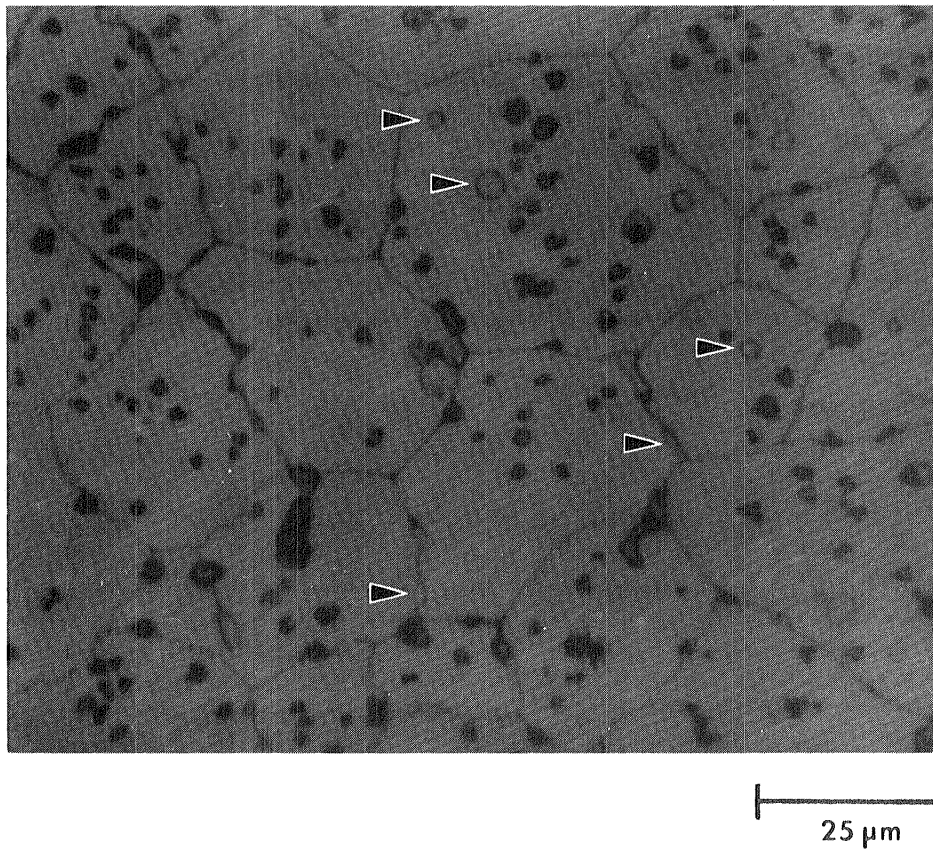
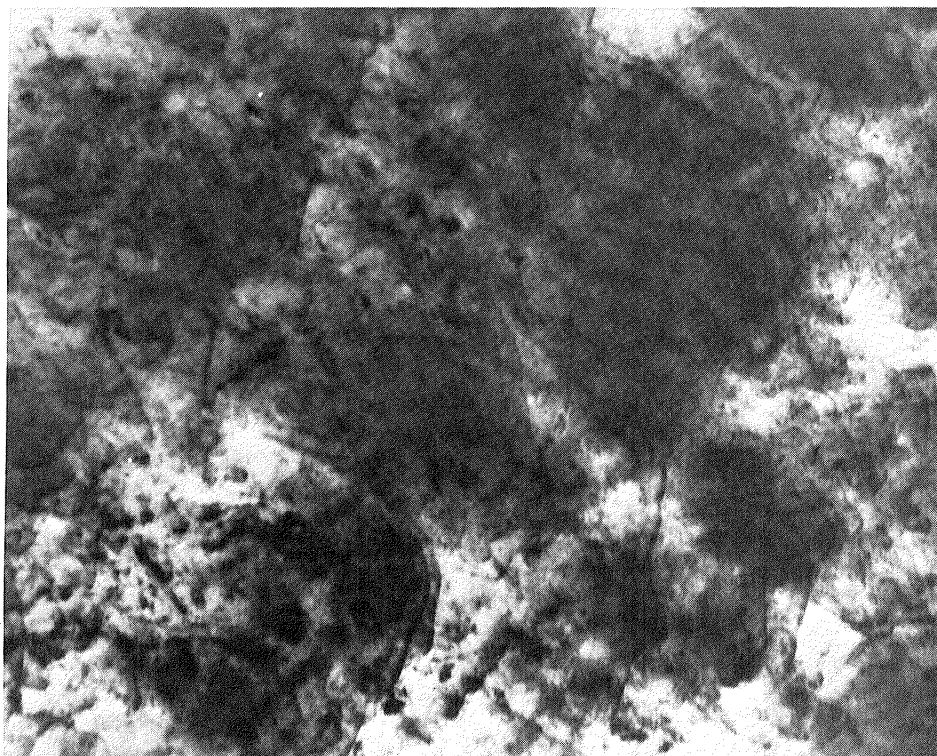


FIGURE 2: Light micrograph showing the commercially produced 4.5 mole-% Y₂O₃-PSZ in the as-received condition. The black areas are pores in the material, and the arrows point to some of the grain boundary and spheroidal precipitates.



BF
multi-beam
 $z = \bar{1}11$
5° off zone

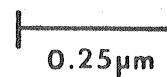
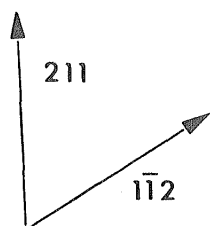


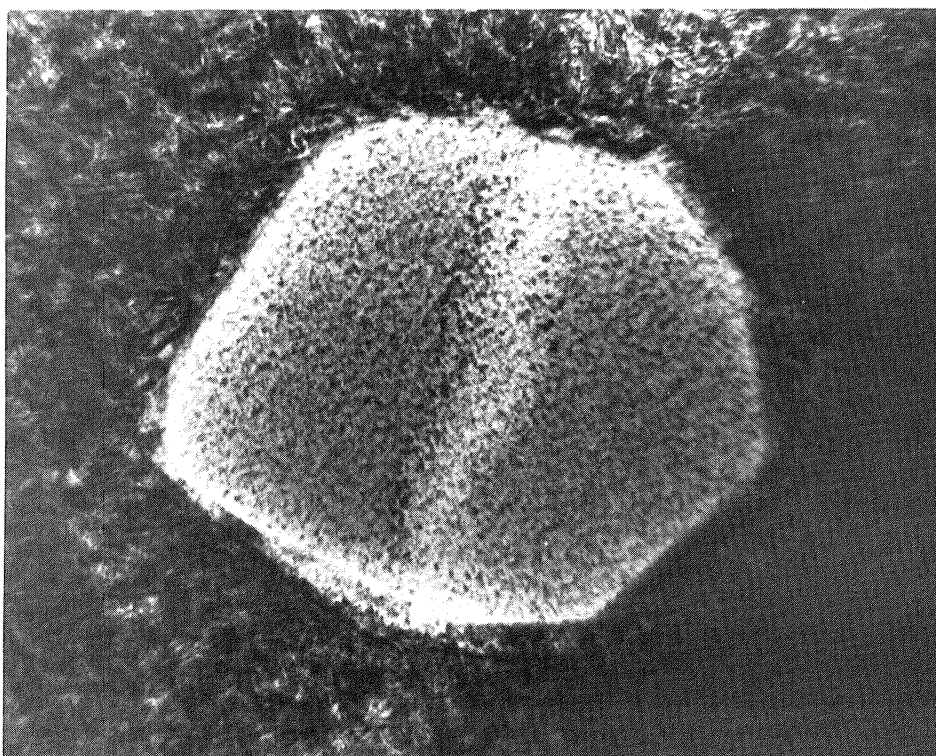
FIGURE 3a: A bright-field TEM of an as-received specimen. In this micrograph, only strain contrast is apparent; in the following micrograph (Figure 3b), the tetragonal precipitates can be observed.



DF
 $\vec{g} = \bar{1}\bar{2}1$
 $z = \bar{1}11$
 5° off zone

0.25 μm

FIGURE 3b: A dark-field TEM of an as-received specimen. In this micrograph, the tetragonal precipitates can be observed. The precipitates are aligned in $\langle 112 \rangle$ directions. The strain fields accompanying the precipitates are shown in the preceding micrograph, Figure 3a.



BF
 $\vec{g} = \bar{2}\bar{2}0$
 $z = \bar{1}11$
 5° off zone

0.25 μm

FIGURE 4: A bright-field TEM of a spheroidal precipitate in an as-received specimen which was oriented in a two-beam condition, with the diffracted beam being the (220) . The mottled, or speckled, appearance of the spheroid is due to damage produced by the ion thinning process used to prepare specimens for the electron microscope.

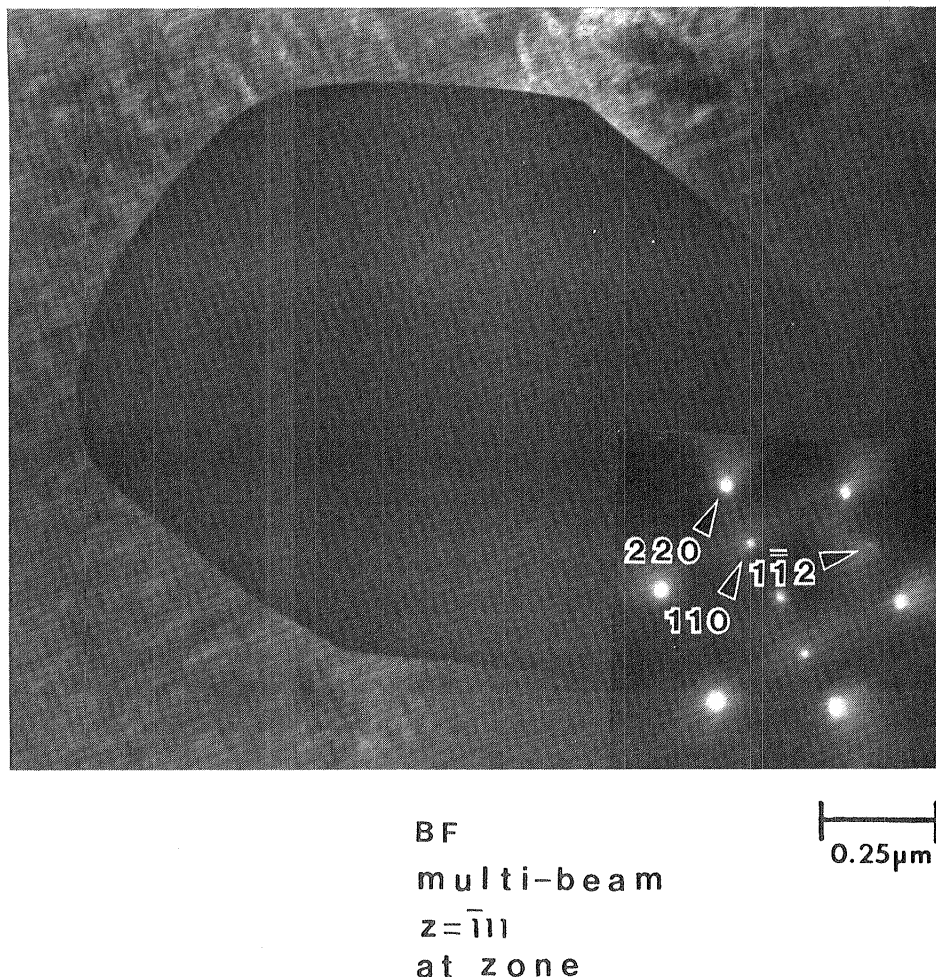


FIGURE 5: A bright-field TEM showing the same spheroidal precipitate that was shown in Figure 4. The precipitate appears dark because it has been tilted to a zone, the $[111]$.

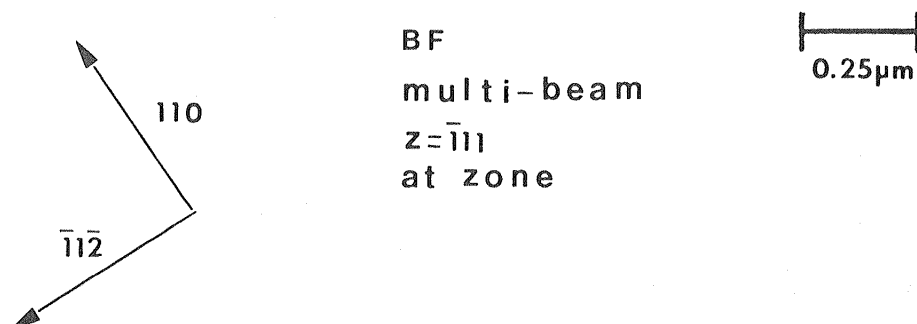
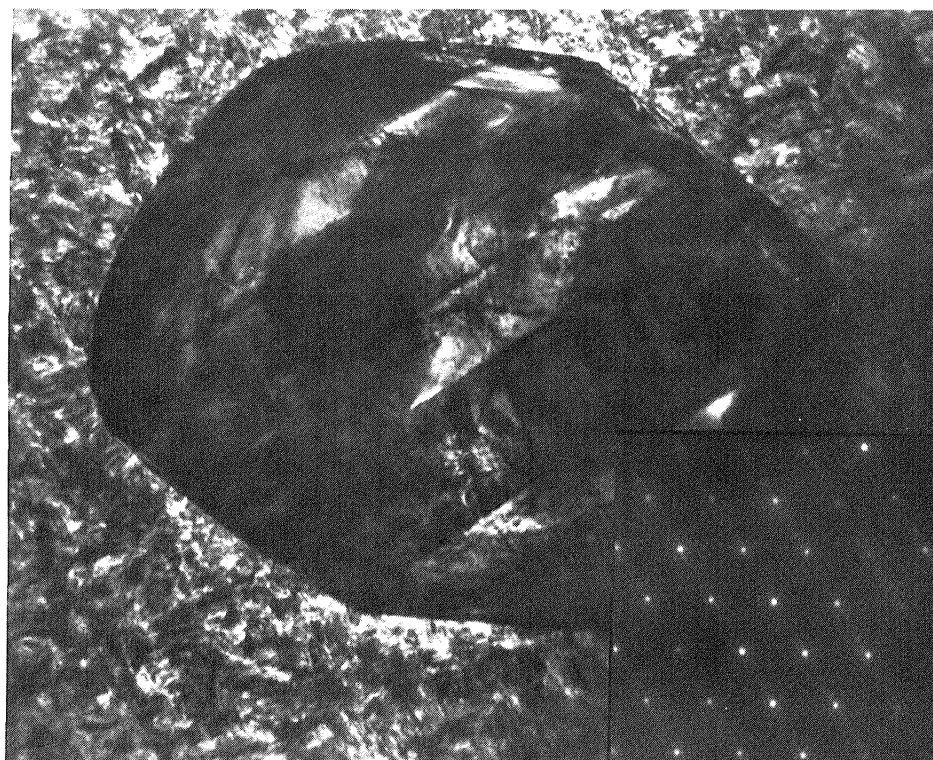


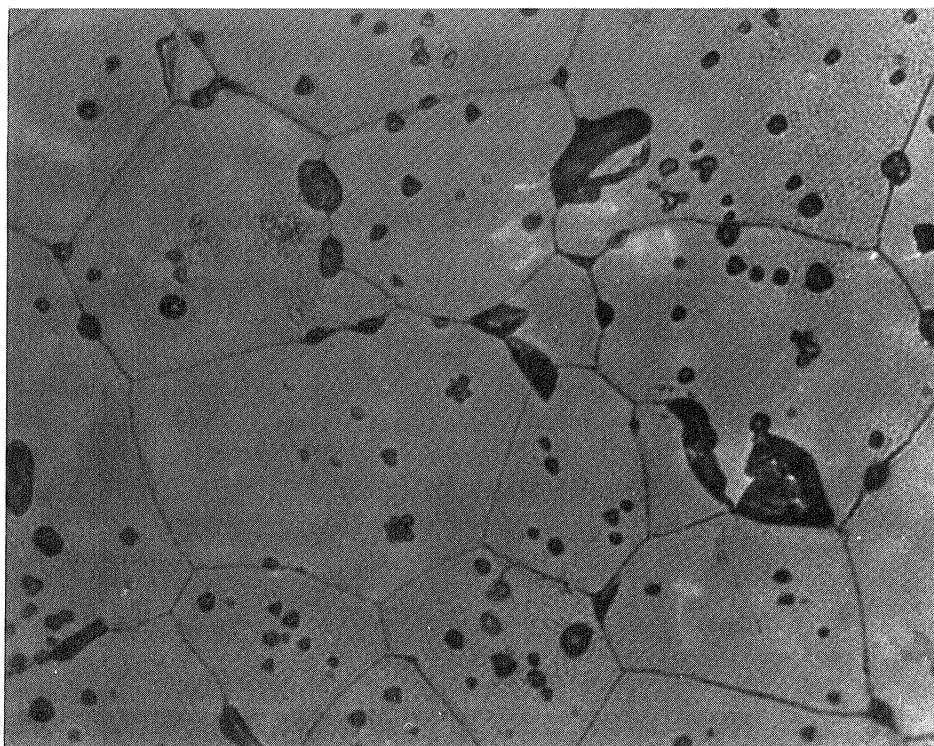
FIGURE 6: A bright-field TEM of the same spheroidal precipitate shown in Figures 4 and 5 after the tetragonal-to-monoclinic transformation. The SAD pattern for the precipitate shows streaking in a $\langle 110 \rangle$ direction because of twins in the particle.



BF

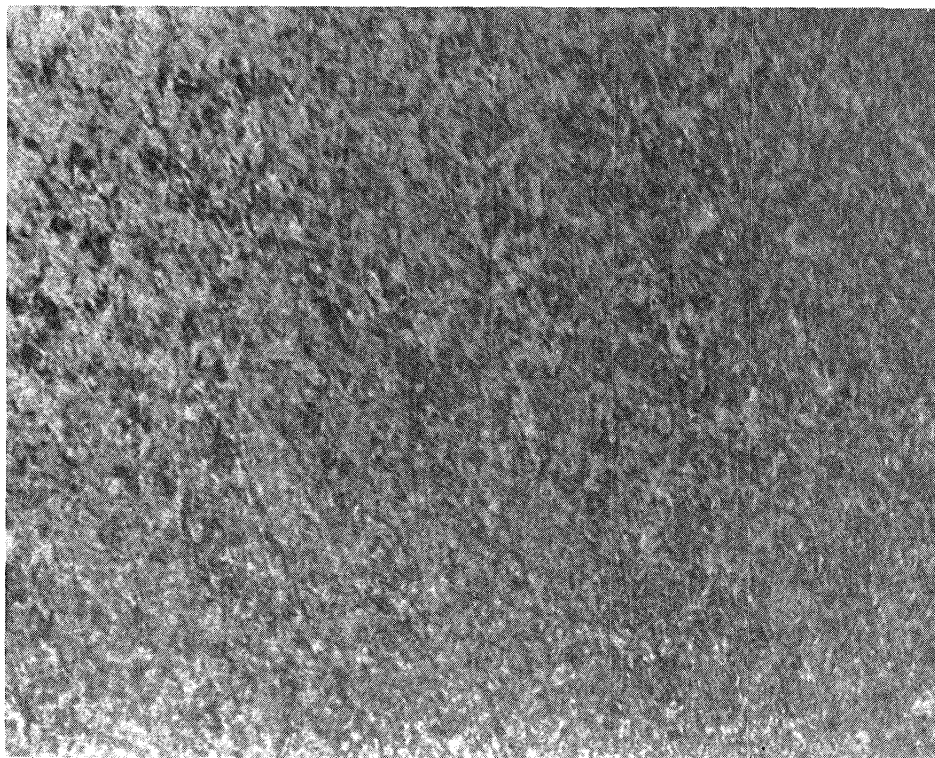
0.25 μ m

FIGURE 7: A bright-field TEM of a grain boundary precipitate found in an as-received specimen. The precipitate has several twins and its SAD pattern showed the streaking associated with the monoclinic twinning.



25 μm

FIGURE 8: Light micrograph showing the Y_2O_3 -PSZ in the solution-annealed-and-quenched condition. The black areas are pores. Note that all of the large precipitates shown in Figure 2 have been dissolved by the solution annealing treatment.



BF

$\bar{g} = \bar{1}\bar{2}1$

$z = \bar{1}11$

5° off zone

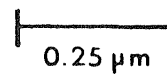
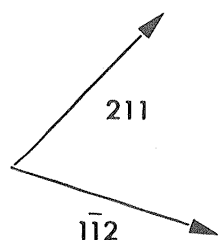
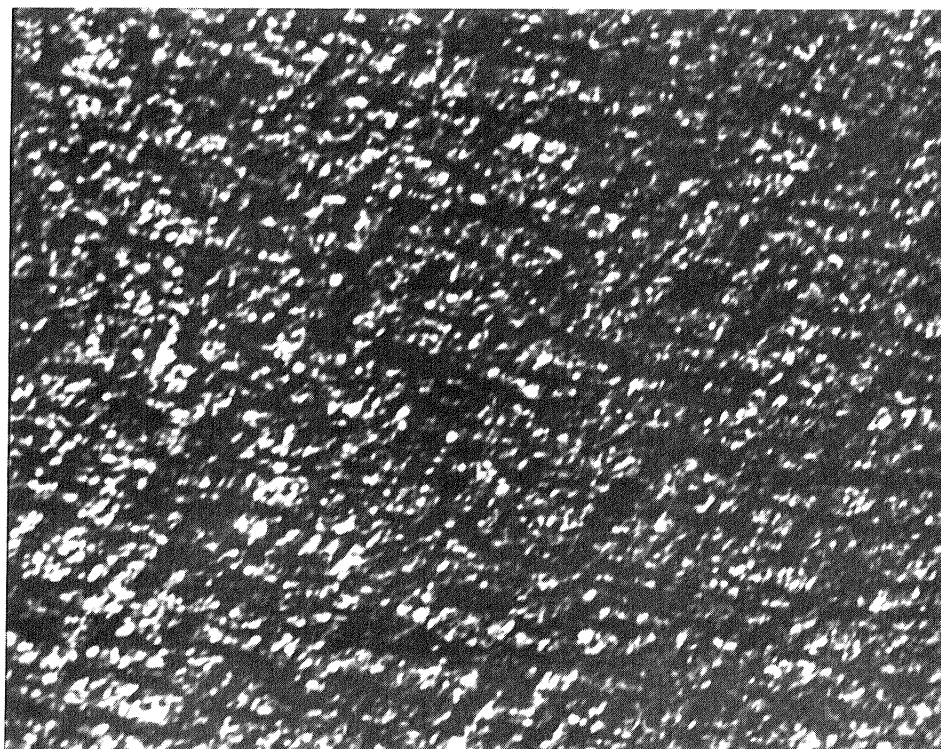


FIGURE 9a: A bright-field TEM of the solution-annealed-and-quenched material. In this micrograph, only strain contrast is observed. The alignment of the precipitates is shown in the dark field micrograph, Figure 9b.



DF
 $\vec{g} = \bar{1}\bar{2}1$
 $z = \bar{1}11$
 5° off zone

0.25 μm

FIGURE 9b: A dark-field TEM of the solution-annealed-and-quenched material showing the alignment of the precipitates. They are aligned in two $\langle 211 \rangle$ directions, yielding a cross-hatched configuration. The strain contrast associated with the precipitates is shown in the previous micrograph, Figure 9a.

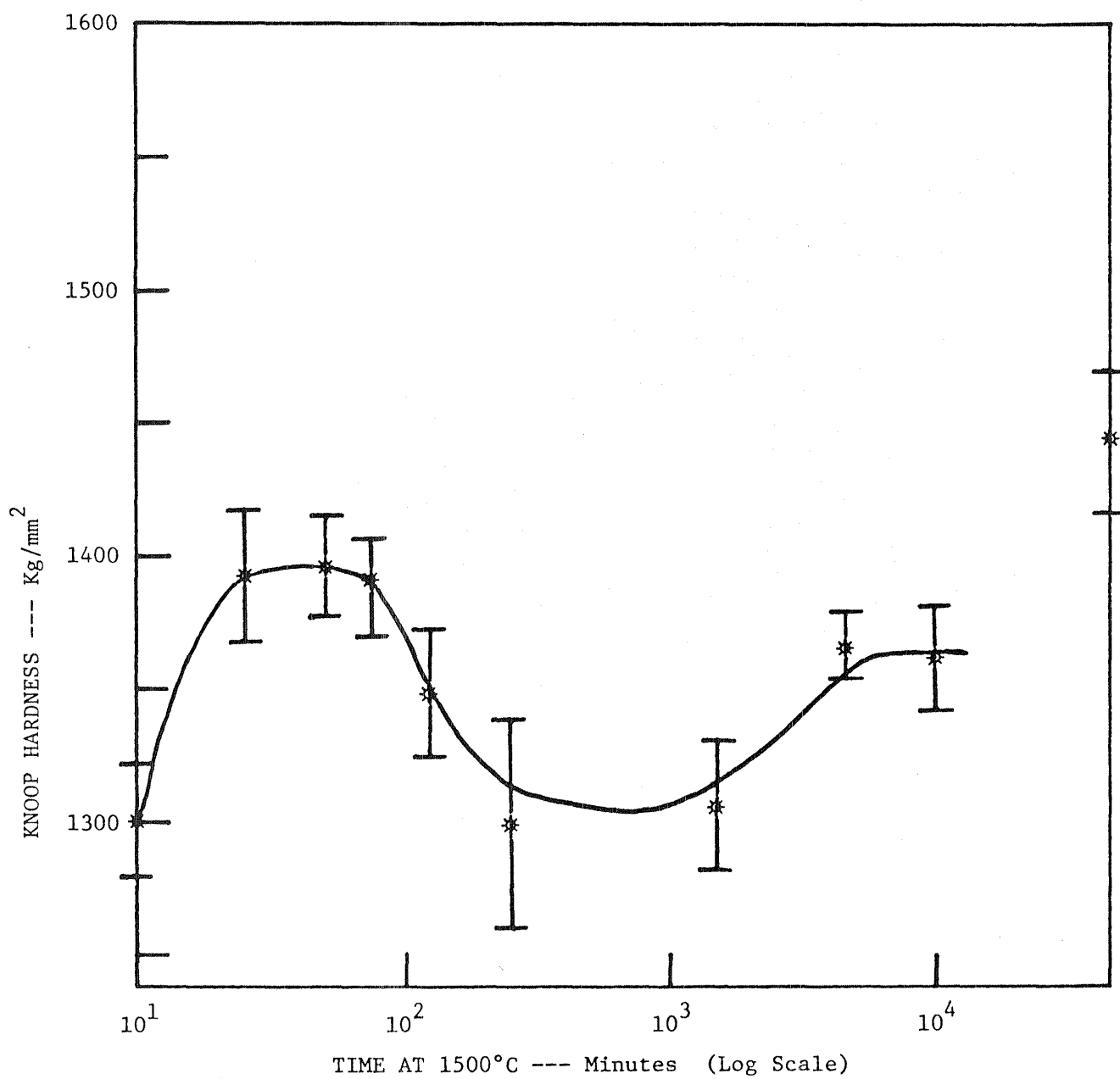
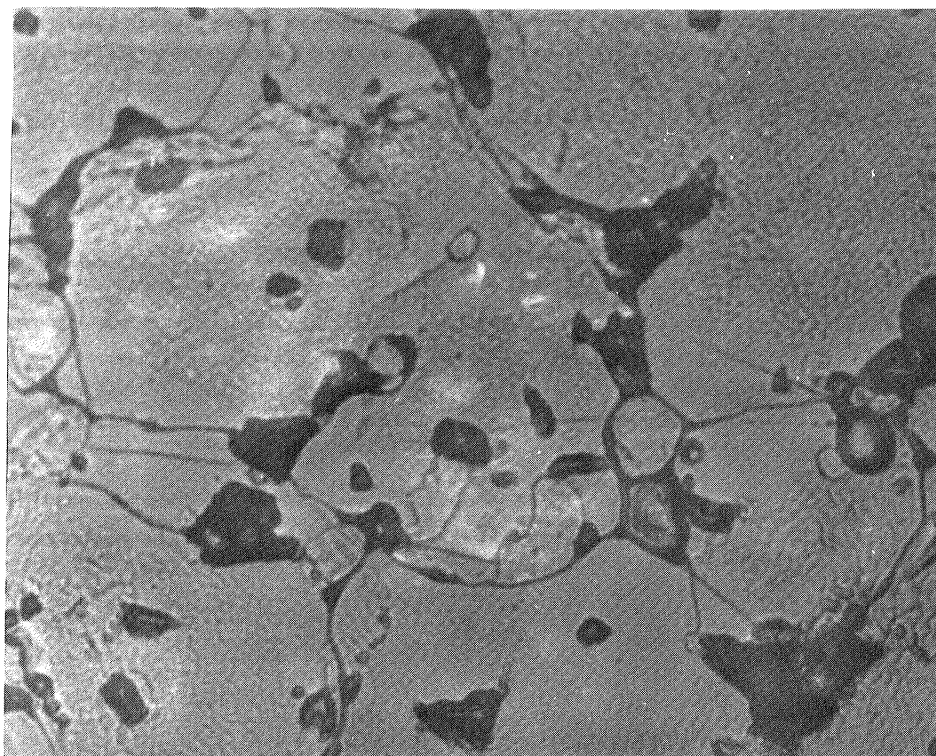
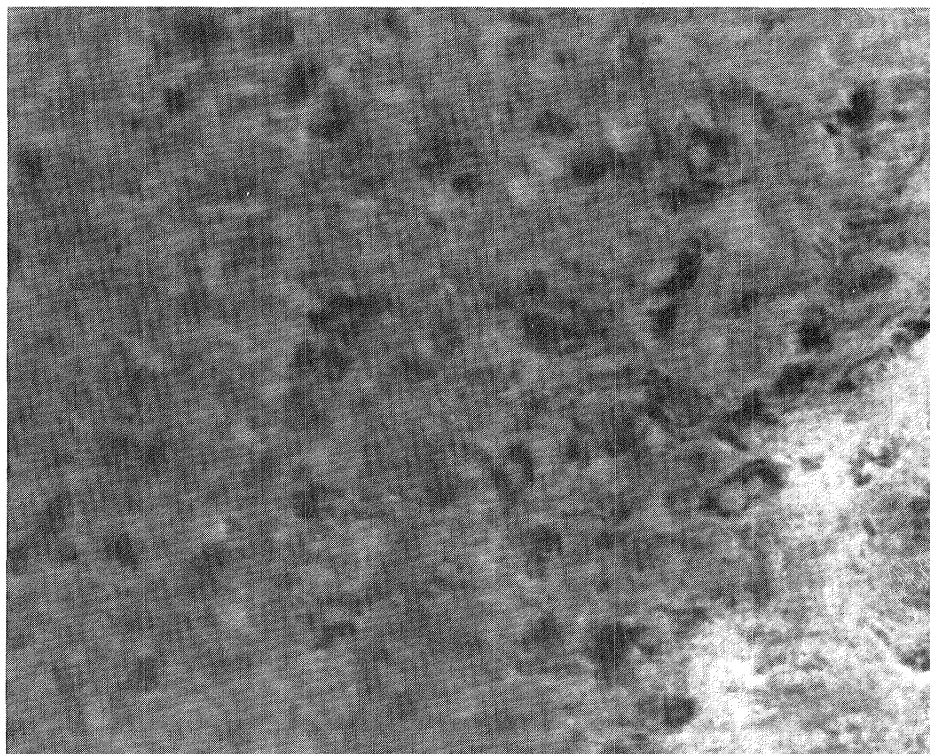


FIGURE 10: Microhardness of the as-received 4.5 mole-% Y_2O_3 - ZrO_2 as a function of aging time at 1500°C. A Knoop diamond indenter, with a 200 gm. load was used in the hardness measurement.



25 μm

FIGURE 11: An optical micrograph of the as-received material after aging for 43,200 minutes at 1500°C. Porosity (black areas) and grain boundary precipitates are quite evident.



BF
 $\vec{g} = \bar{2}3\bar{1}$
 $z = 013$
 3° off zone

0.15μm

FIGURE 12a: Transmission electron micrograph of an as-received specimen, taken with in the bright-field mode, showing only strain contrast around precipitate particles. The dark field mode micrograph of the same area of the specimen is shown in the next figure, Figure 12b.

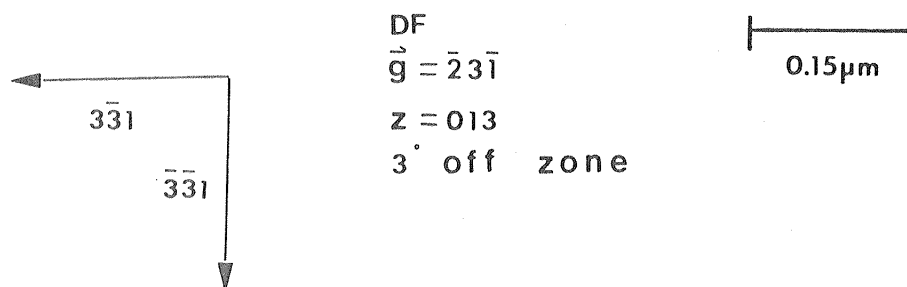


FIGURE 12b: A dark-field electron micrograph of the same area of the as-received specimen shown in Figure 12a. The tetragonal precipitates are clearly visible in the micrograph; they are aligned in two $\langle 3\bar{3}1 \rangle$ directions (approximately). The dark field image was produced using a (231) fluorite-forbidden reflection, which arises only from the tetragonal phase, and not from the cubic phase.

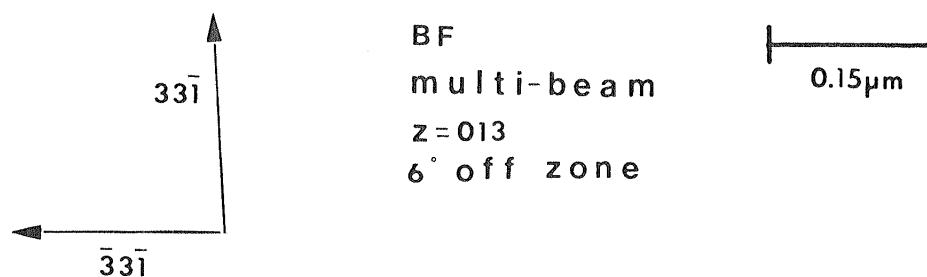
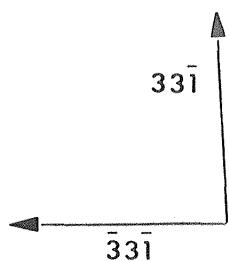
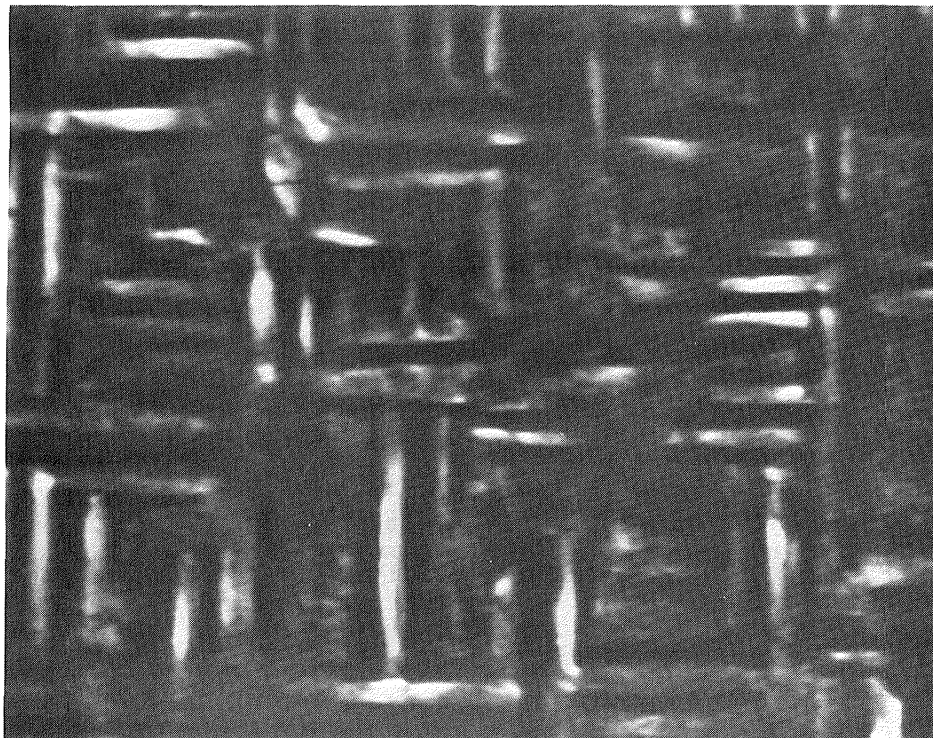


FIGURE 13a: Bright-field TEM of an area of the as-received material aged for 250 minutes at 1500°C. a $\{100\}$ reflection, resulting from double diffraction from $\{300\}$ and $\{310\}$ fluorite-forbidden reflections, was used to form the image. The precipitates are shown to lie along two $\langle 331 \rangle$ directions.



DF
 $\vec{g} = \bar{1}00$
 $z = 013$
 8° off zone

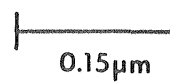


FIGURE 13b: Dark-field TEM of the same specimen shown in Figure 13a. Please refer to Figure 13a for imaging details.

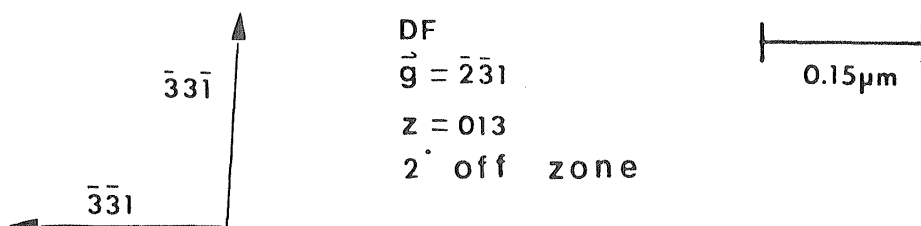
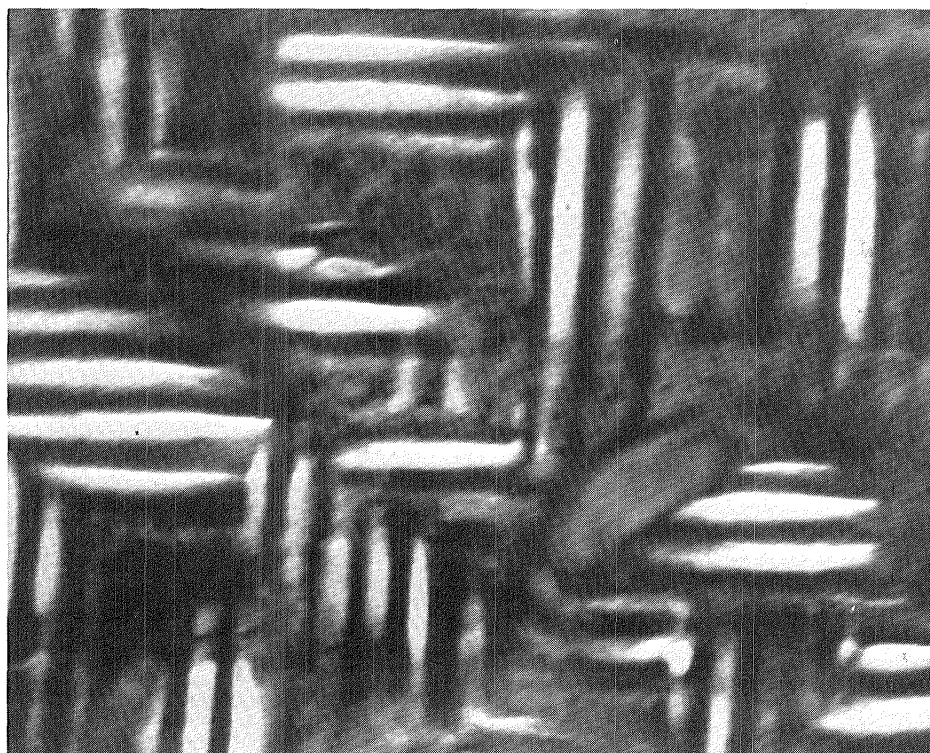
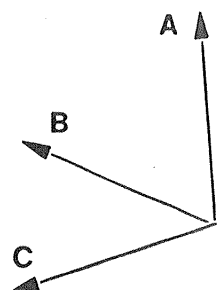


FIGURE 14: A dark-field TEM of an as-received specimen that was aged for 1,525 minutes at 1500°C. The precipitates are shown aligned in $\langle 331 \rangle$ directions. Note how the precipitates are grouping together to form particles made up of alternating tetragonal variants.



BF
multi-beam

0.25 μ m

FIGURE 15a: A bright-field TEM of a grain boundary precipitate in an as-received specimen that had been aged for 1,525 minutes at 1500°C. The three directions, A, B, and C are normals to the twin planes. Note the crack in the upper right portion of the image area.

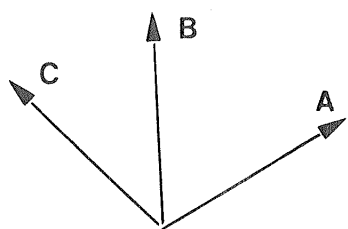
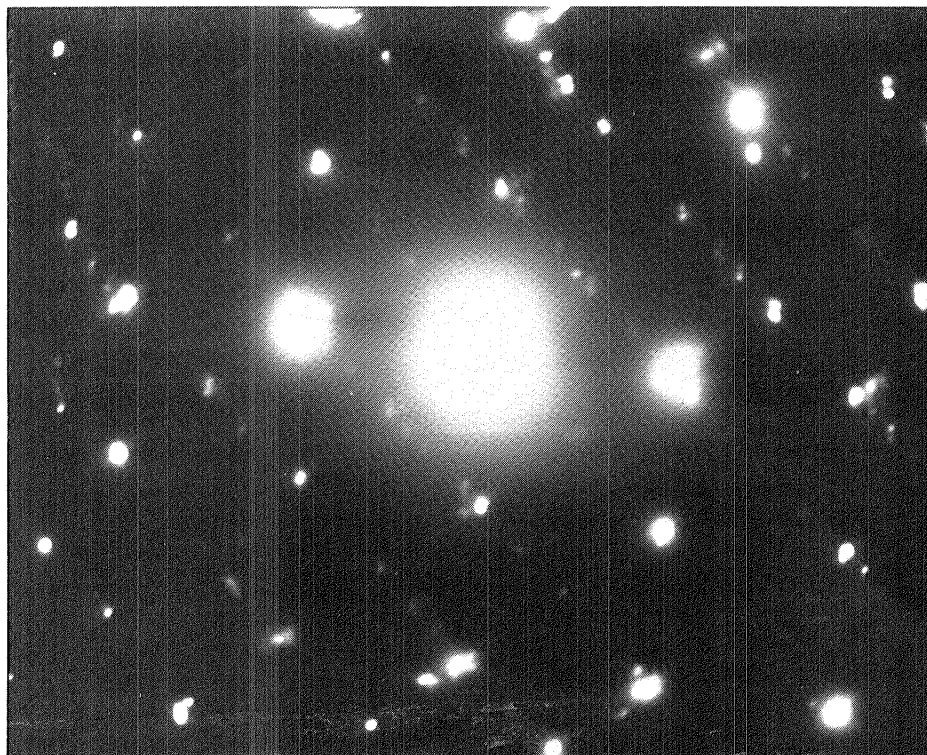


FIGURE 15b: A diffraction pattern of the same specimen shown in Figure 15a. The three directions, A, B, and C are the directions in which streaking occurred. Please refer to Figure 15a for the TEM of the specimen.

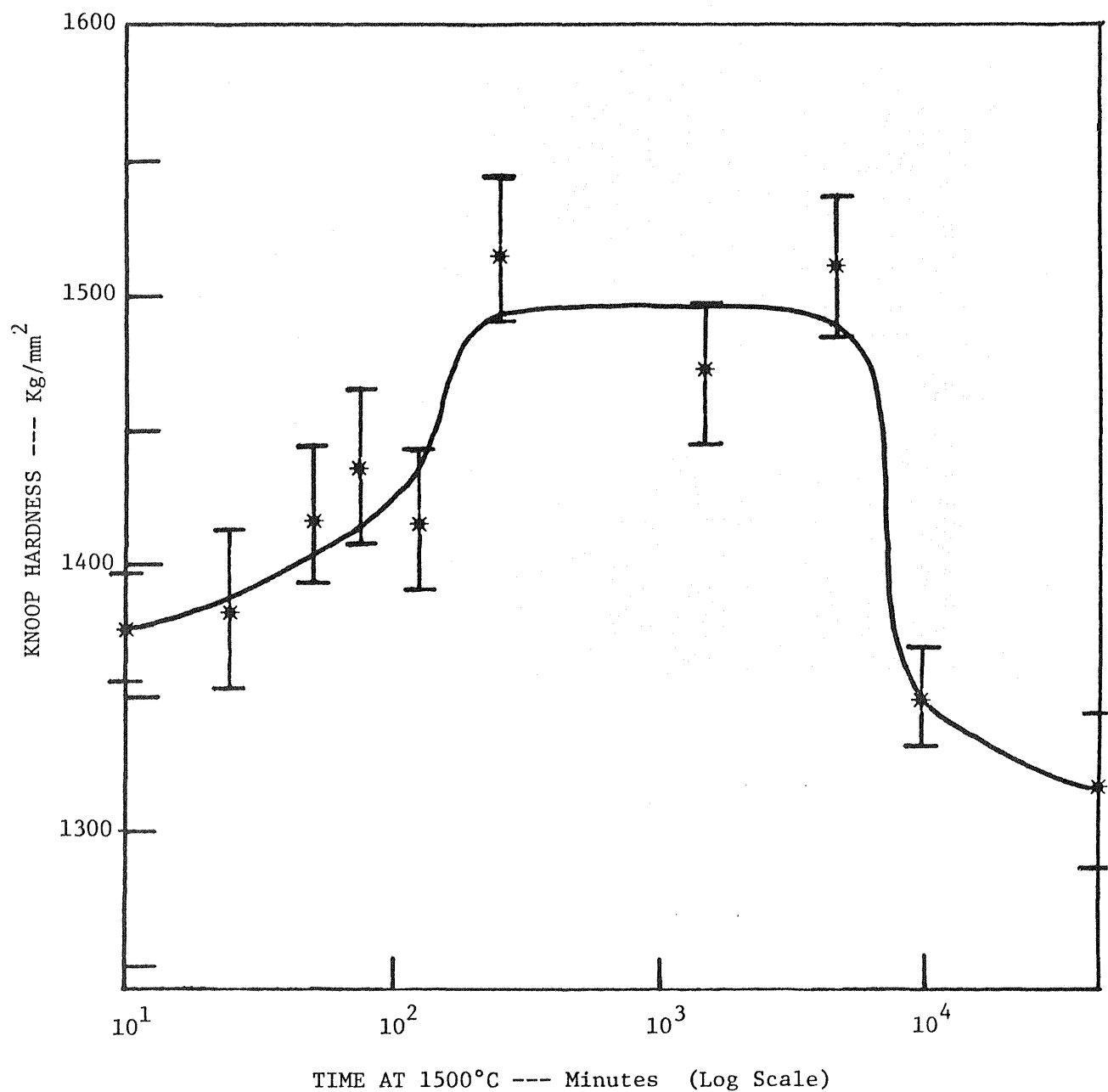


FIGURE 16: Microhardness of the solution-annealed-and-quenched 4.5 mole-% Y_2O_3 - ZrO_2 as a function of aging time at 1500°C. A Knoop diamond indenter with a 200 gm load was used for the hardness measurements.

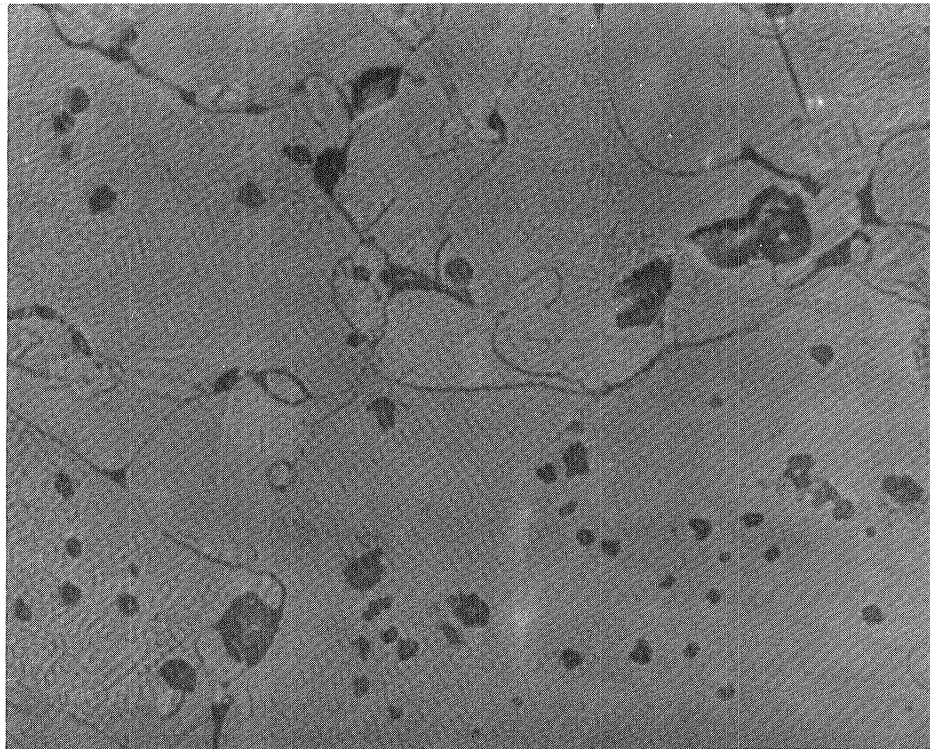


FIGURE 17: An optical micrograph of a solution-annealed-and-quenched specimen that was aged for 43,200 minutes at 1500°C. This specimen was found to have a large number of grain boundary precipitates.

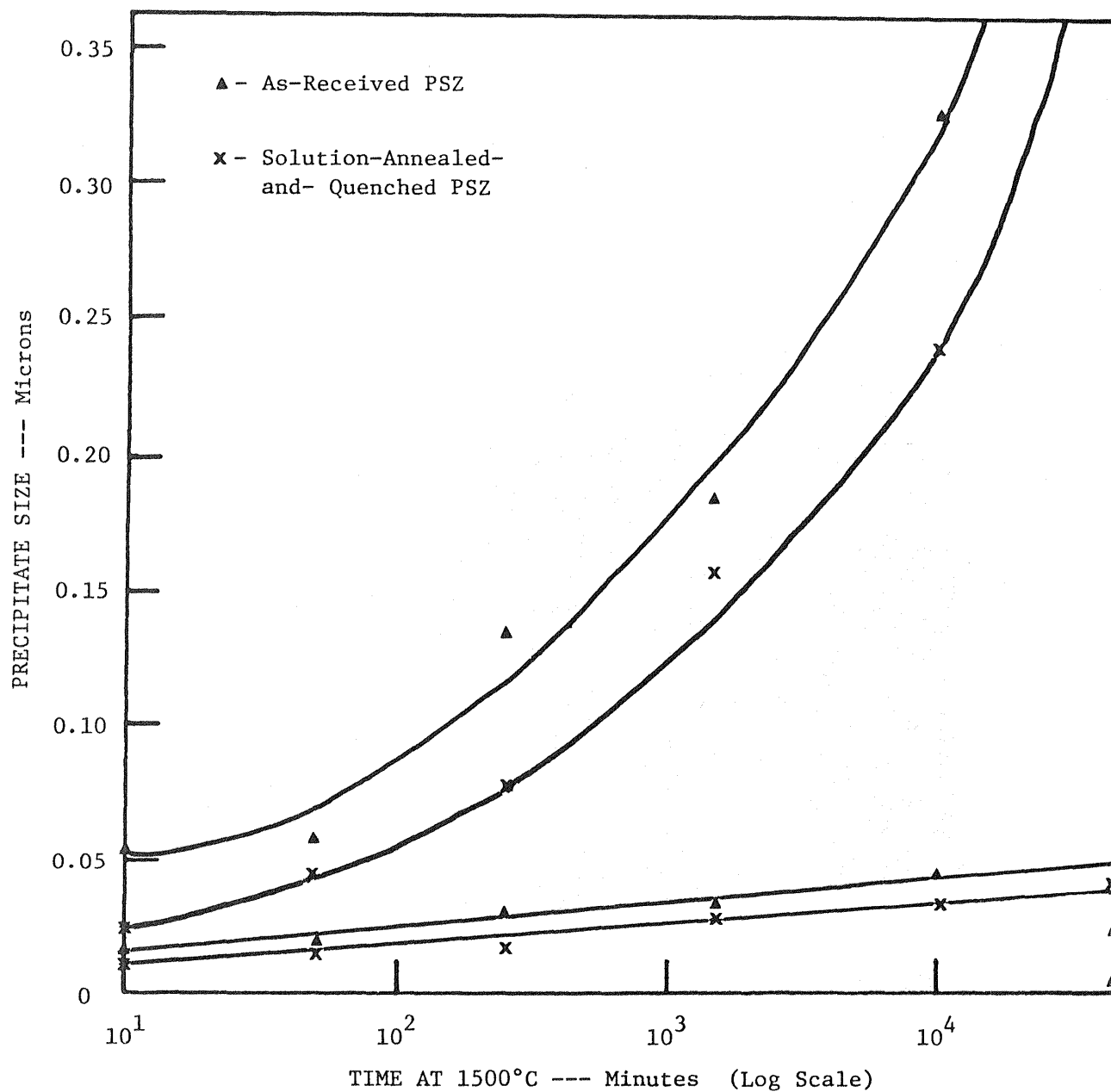


FIGURE 18: Tetragonal precipitate growth of the solution-annealed-and-quenched and of the as-received PSZ as functions of aging time at 1500°C. Precipitate sizes were measured in two orthogonal directions.

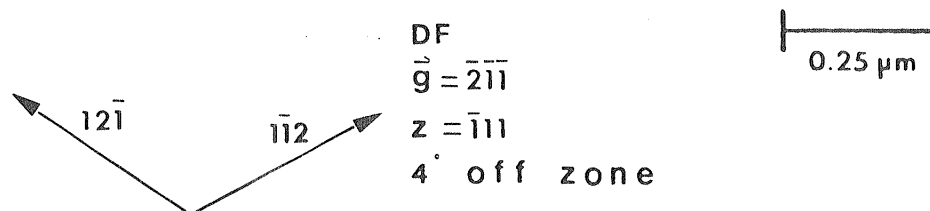
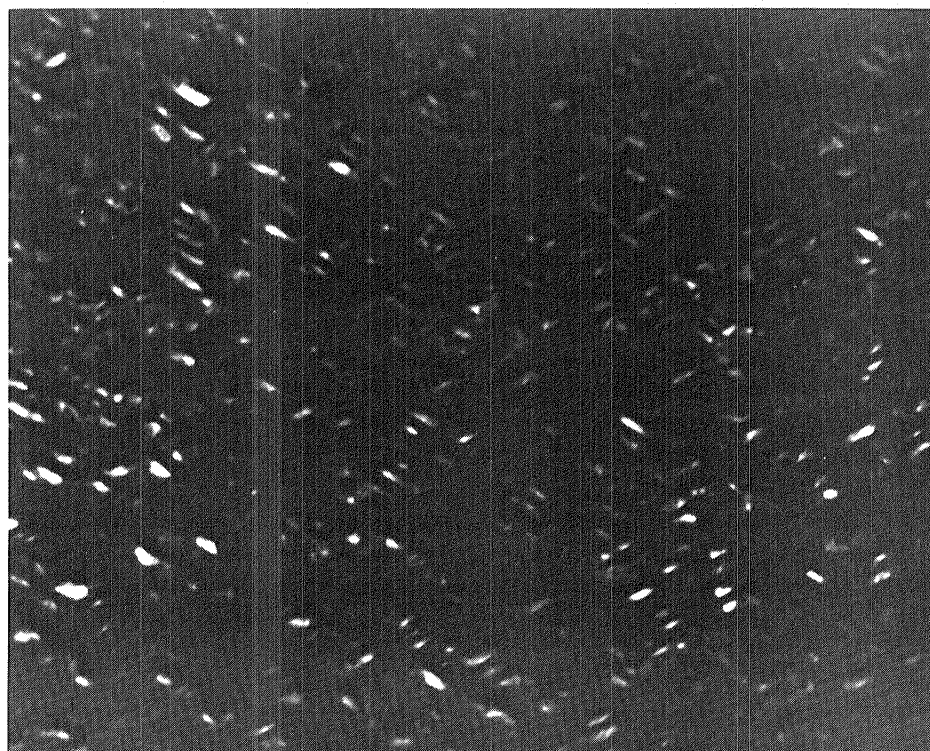


FIGURE 19: A dark-field TEM of the as-received material aged for 50 minutes at 1500°C. Precipitates are shown aligned in two $\langle 112 \rangle$ directions.

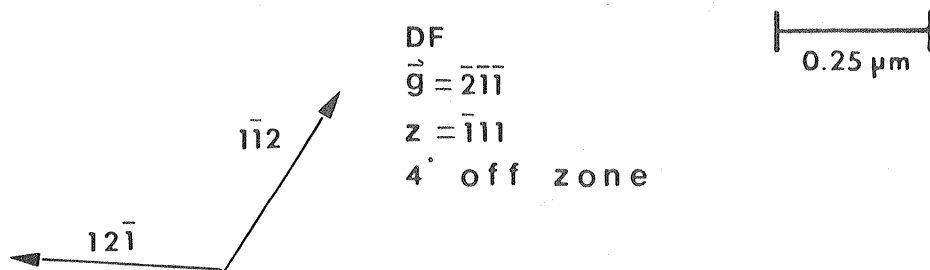
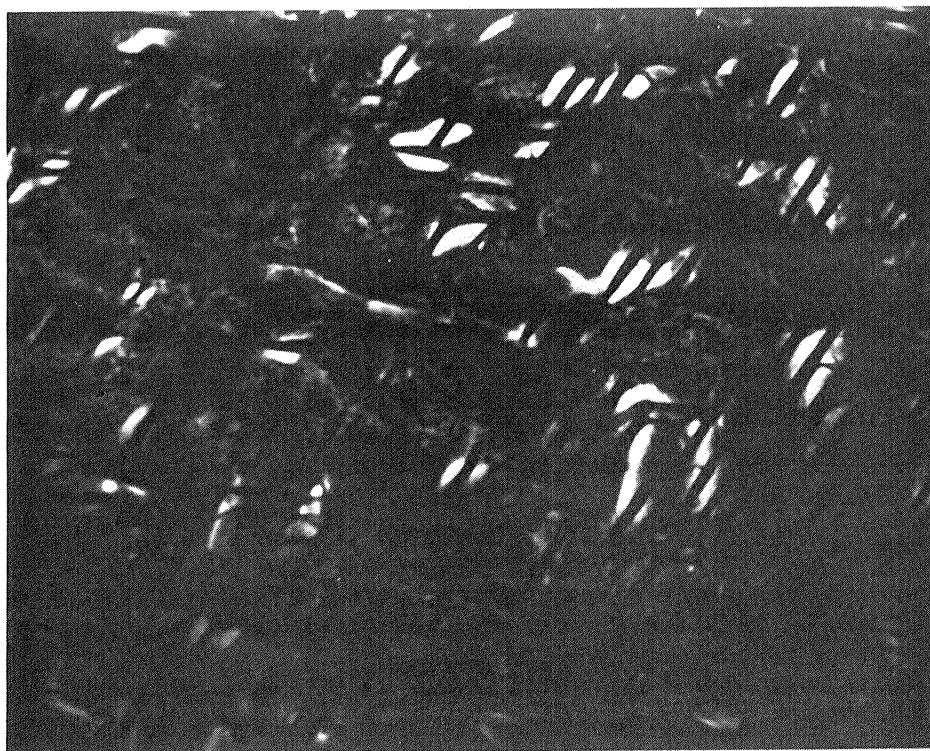


FIGURE 20: A dark-field TEM of the as-received material aged for 250 minutes at 1500°C. Precipitates are shown aligned in two $\langle 112 \rangle$ directions.

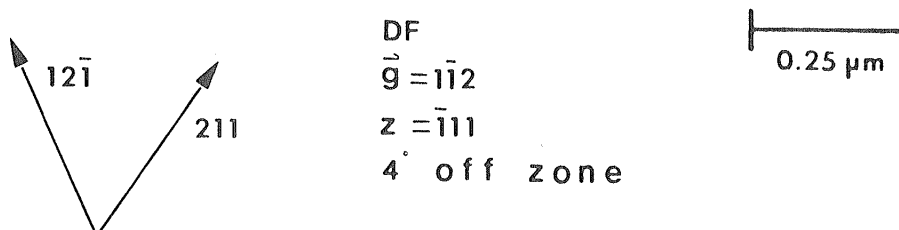
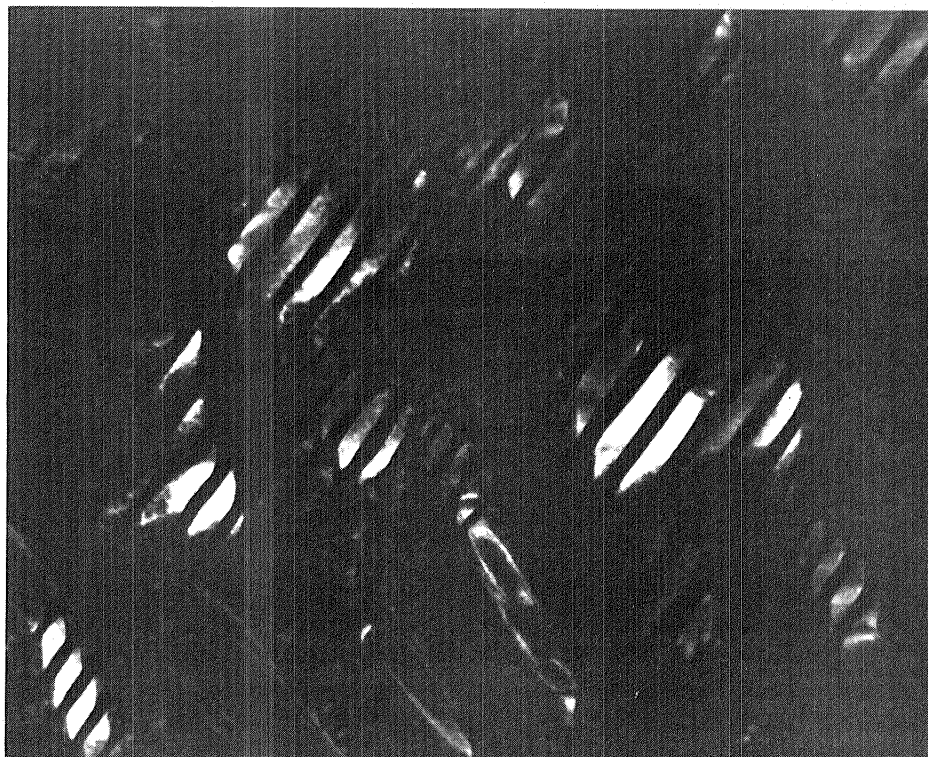
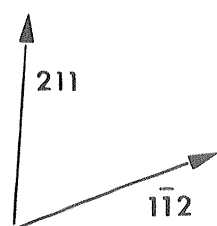
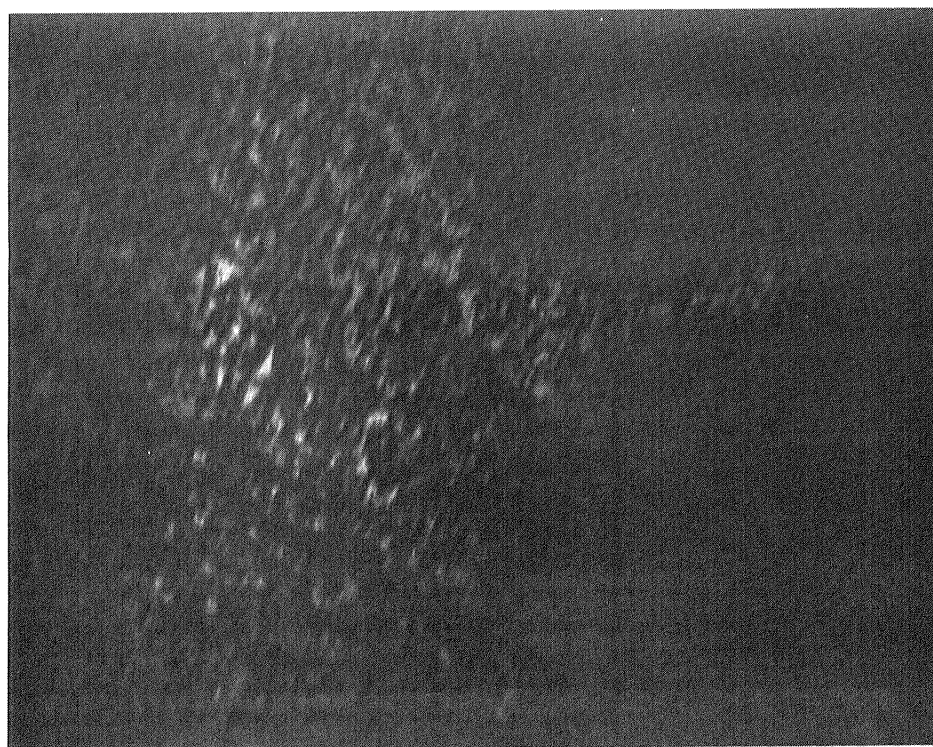


FIGURE 21: A dark-field TEM of the as-received material aged for 10,080 minutes at 1500°C. Precipitates are shown aligned in two $\langle 112 \rangle$ directions.



DF
 $\vec{g} = 12\bar{1}$
 $z = \bar{1}11$
 3° off zone

0.25 μm

FIGURE 22a: A dark-field TEM of an as-received specimen aged for 43,200 minutes at 1500°C . The precipitates are shown aligned in two $\langle 112 \rangle$ directions.



BF
multi-beam
 $z = \bar{1}11$
3° off zone

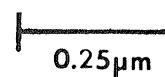
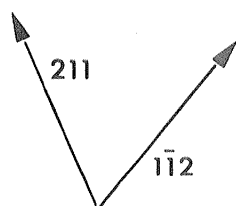
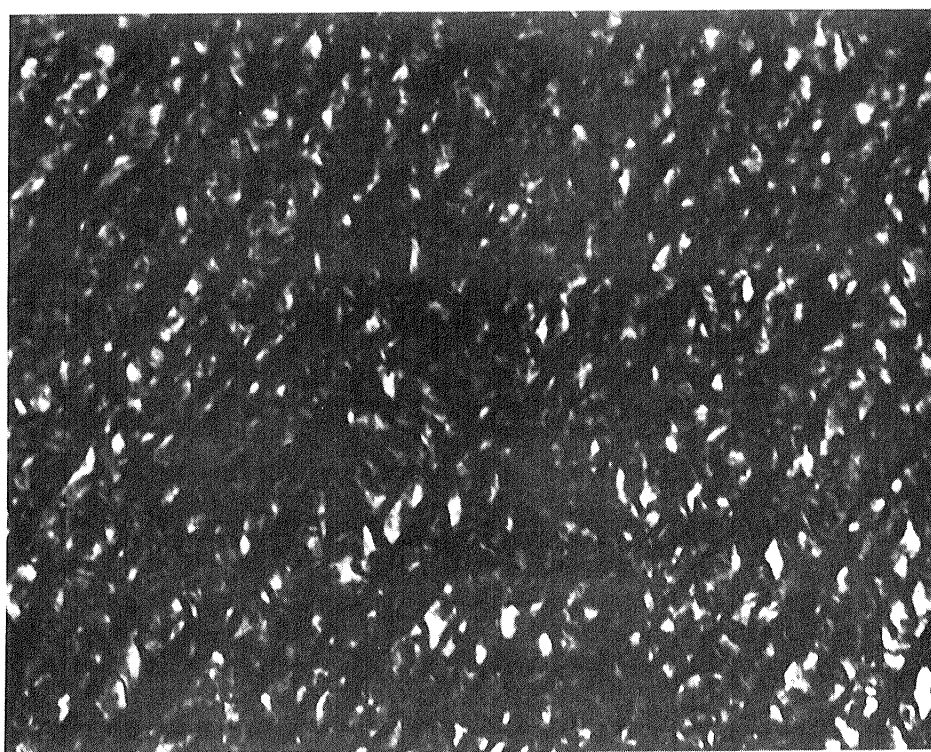


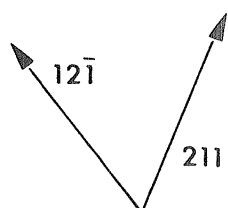
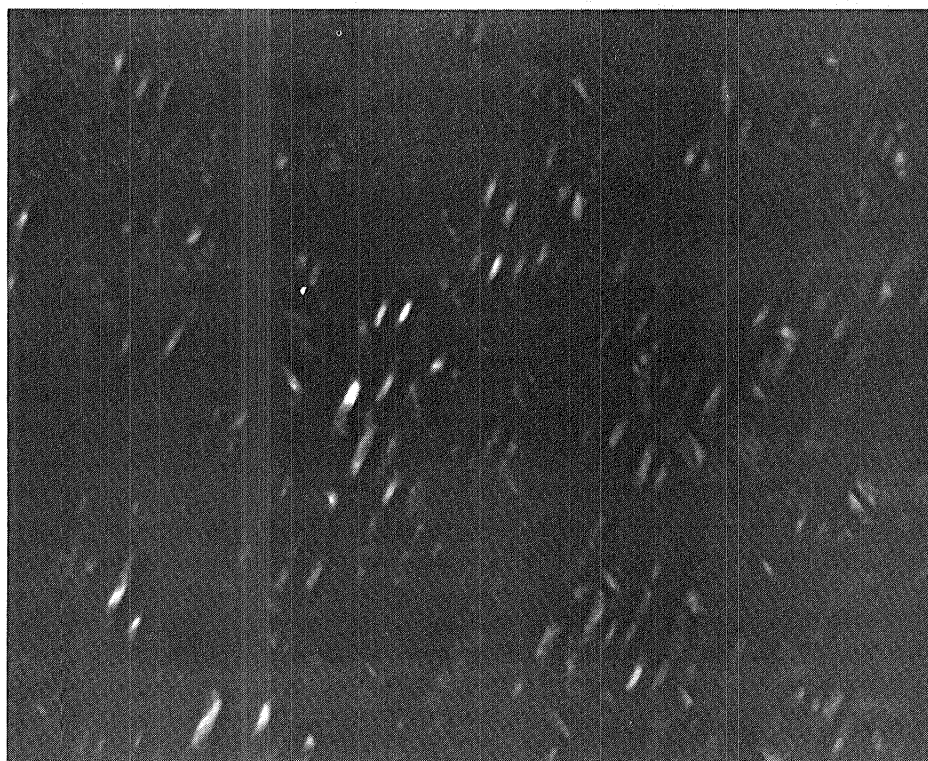
FIGURE 22b: A bright-field TEM of an as-received specimen aged for 43,200 minutes at 1500°C (same specimen as that represented in Figure 22a). Only strain contrast and bend contours are visible in the micrograph.



DF
 $\vec{g} = \bar{1}\bar{2}1$
 $z = \bar{1}11$
 7° off zone

0.25 μm

FIGURE 23: A dark-field TEM of the solution-annealed-and-quenched material aged at 1500°C for 50 minutes. The precipitates are shown to lie along two $\langle 112 \rangle$ directions.



DF
 $\vec{g} = \bar{1}1\bar{2}$
 $z = \bar{1}11$
 7° off zone

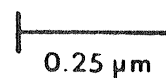
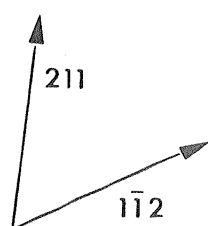
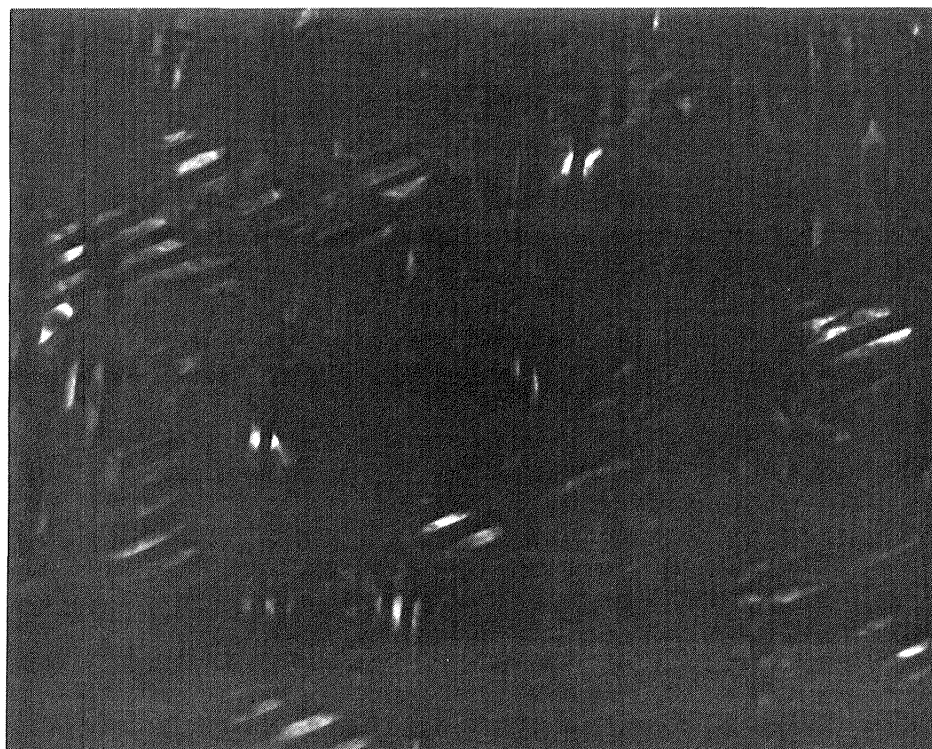


FIGURE 24: A dark-field TEM of the solution-annealed-and-quenched material aged at 1500°C for 250 minutes. The precipitates are shown to lie along two $\langle 112 \rangle$ directions.



DF
 $\vec{g} = 12\bar{1}$
 $z = \bar{1}11$
 4° off zone

0.25 μm

FIGURE 25: A dark-field TEM of the solution-annealed-and-quenched material aged at 1500°C for 1,525 minutes. The precipitates are shown to lie along two $\langle 112 \rangle$ directions.

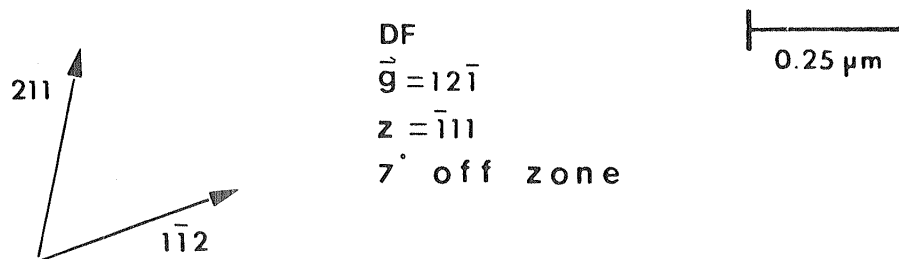
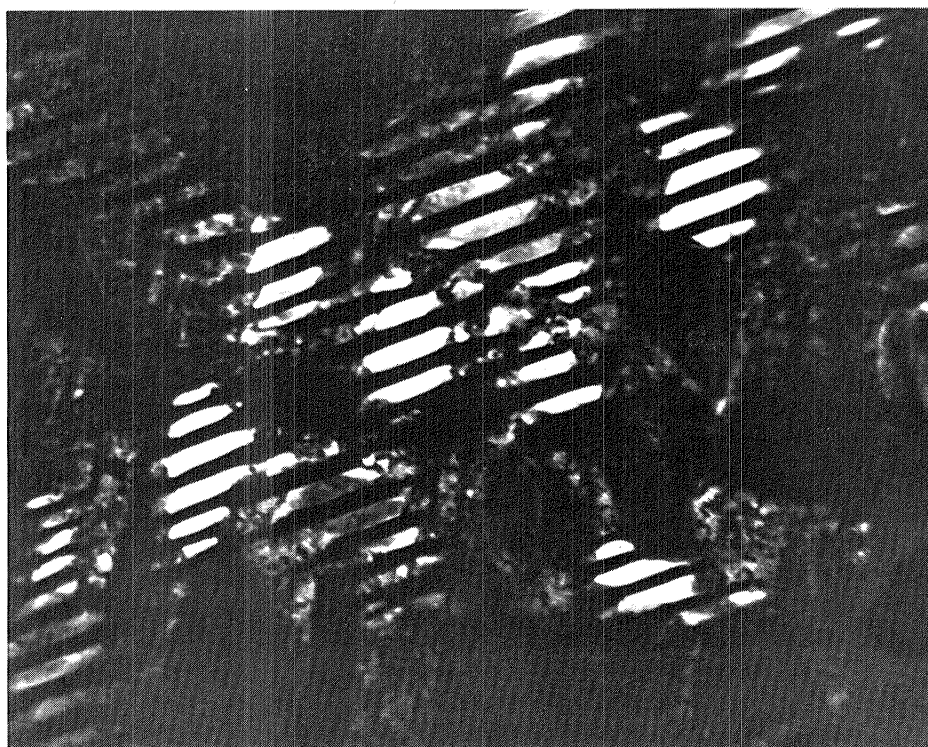
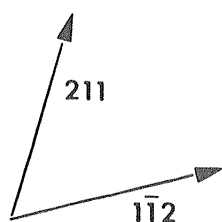
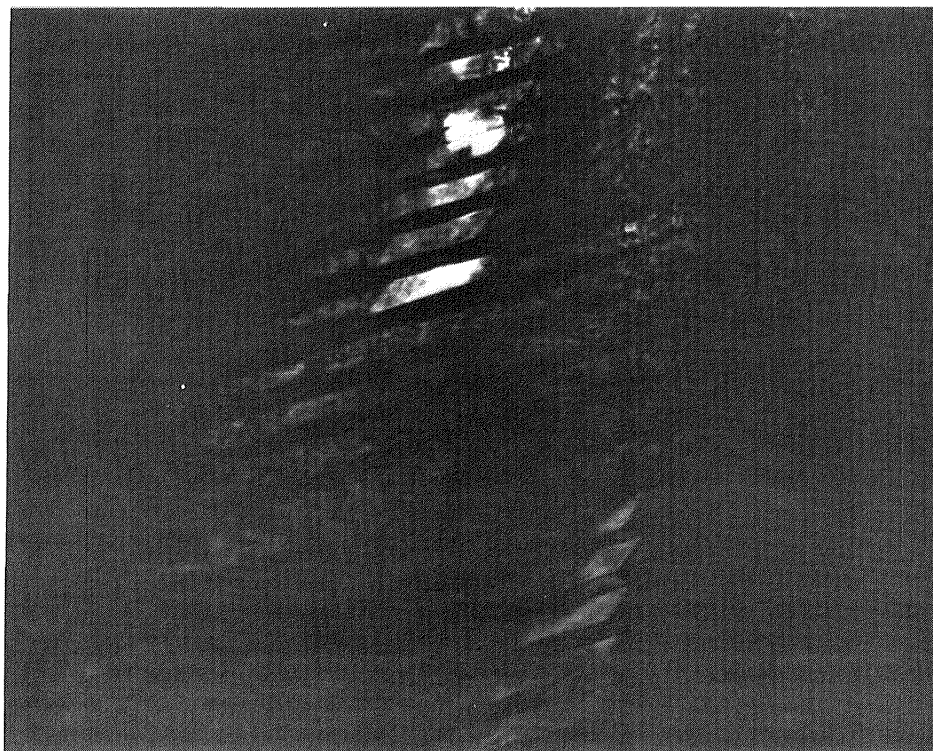


FIGURE 26: A dark-field TEM of the solution-annealed-and-quenched material aged at 1500°C for 10,080 minutes. The precipitates are shown to lie along two $\langle 112 \rangle$ directions.



DF
 $\vec{g} = \bar{1}\bar{2}1$
 $z = \bar{1}11$
 4° off zone

0.25 μm

FIGURE 27: A dark-field TEM of the solution-annealed-and-quenched material aged at 1500°C for 43,200 minutes. The precipitates are shown to lie along two $\langle 112 \rangle$ directions.

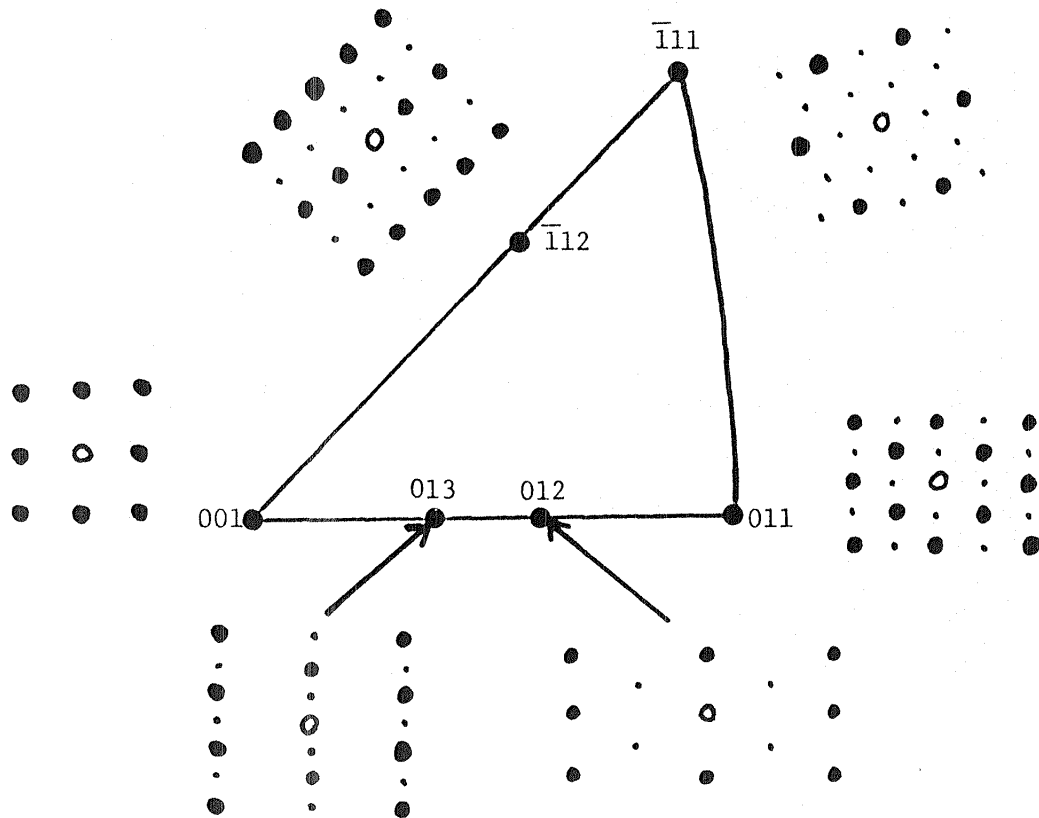


FIGURE 28: The unit stereographic triangle for cubic (fcc) zirconia with tetragonal precipitates. Shown are the locations for the $[013]$, $[012]$, $[011]$, $[\bar{1}11]$, $[\bar{1}12]$, and $[001]$ zones, and their associated diffraction patterns.

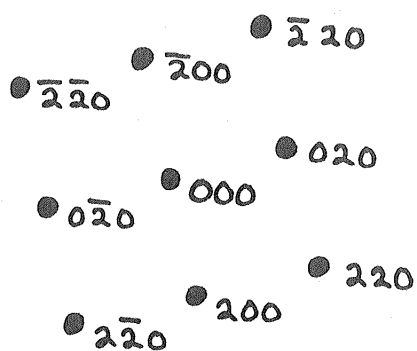
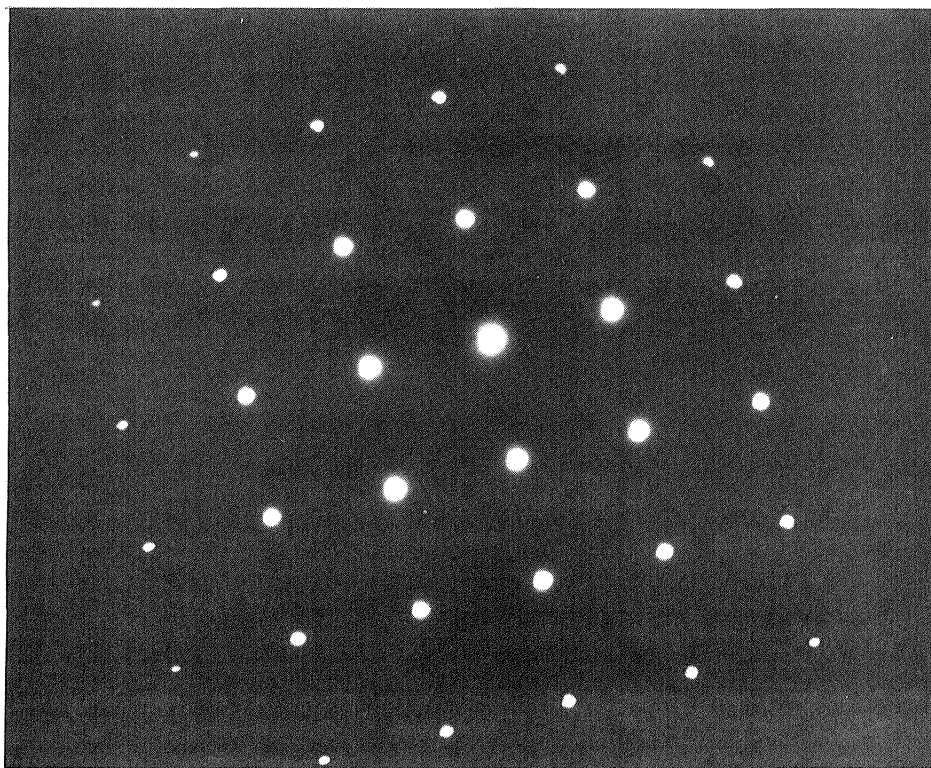


FIGURE 29a: Typical SAD pattern for aged and unaged specimens.
The pattern shown is that of a [001] zone.

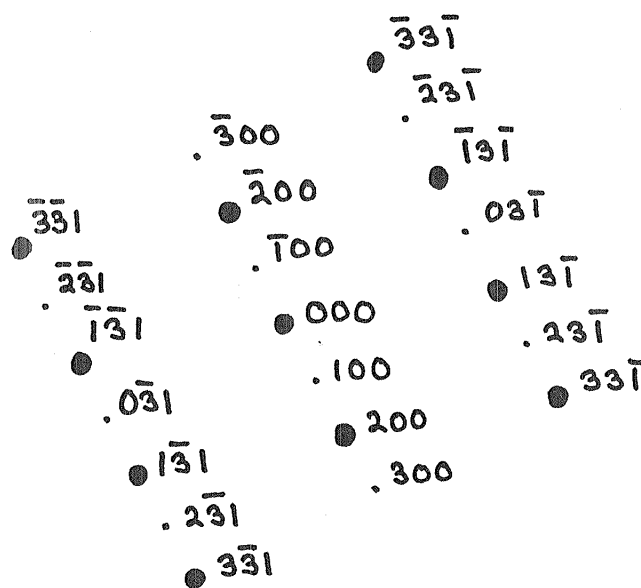
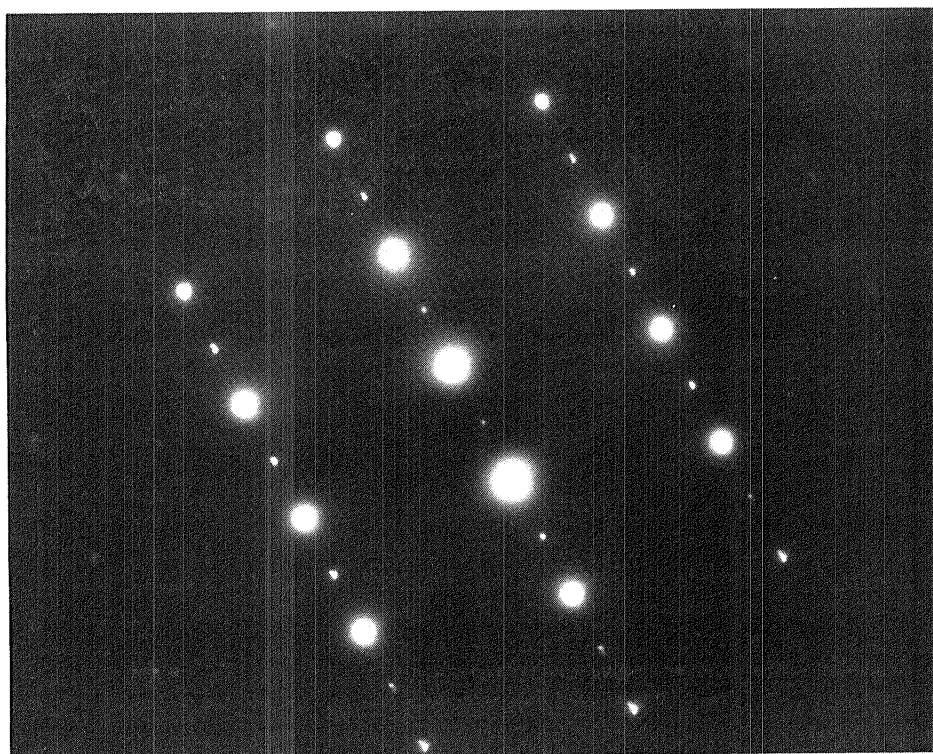


FIGURE 29b: Typical SAD pattern for aged and unaged specimens. The pattern shown is that of a $[013]$ zone.

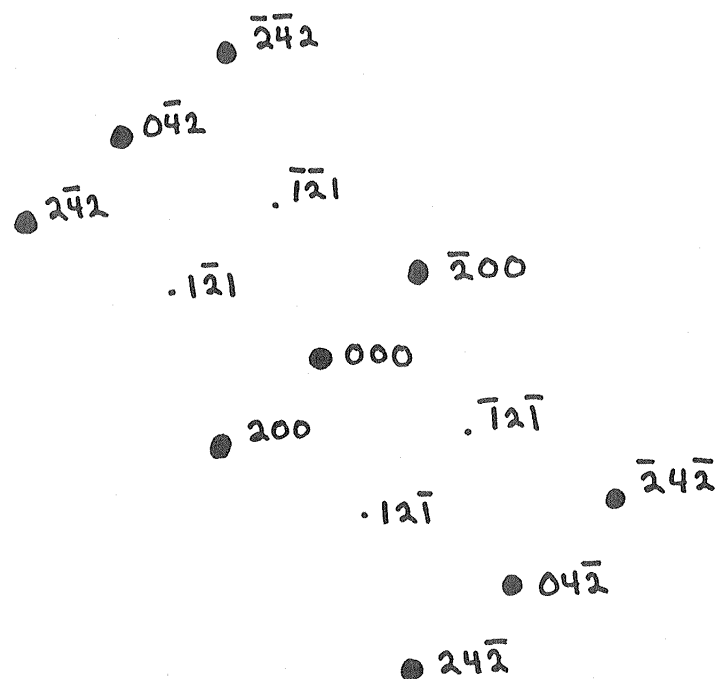
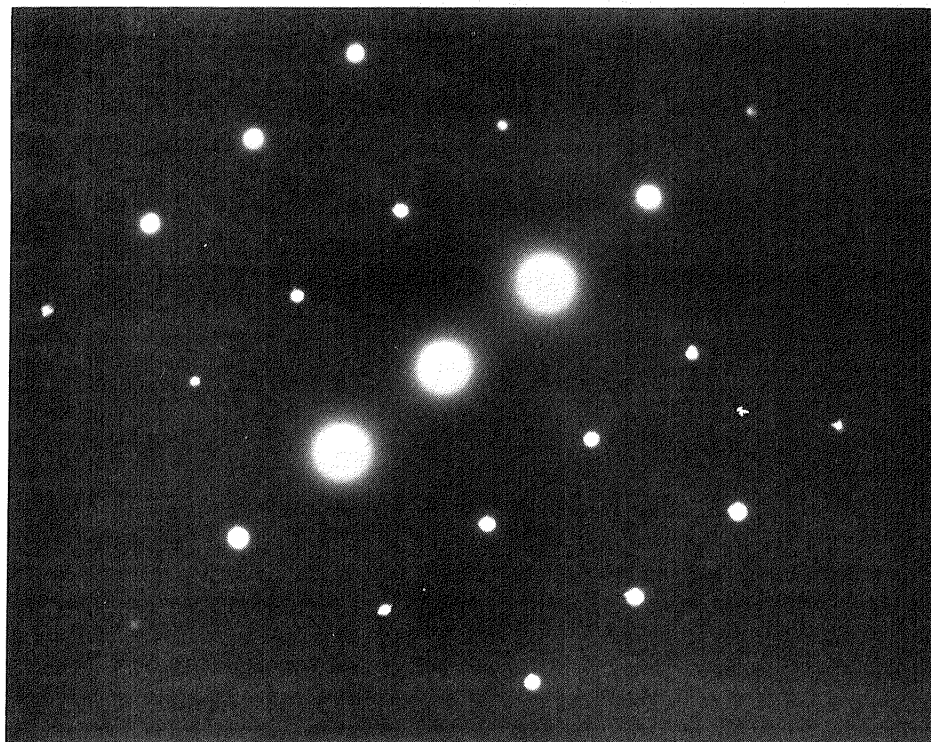


FIGURE 29c: Typical SAD pattern for aged and unaged specimens. Pattern shown is that of a $[012]$ zone.

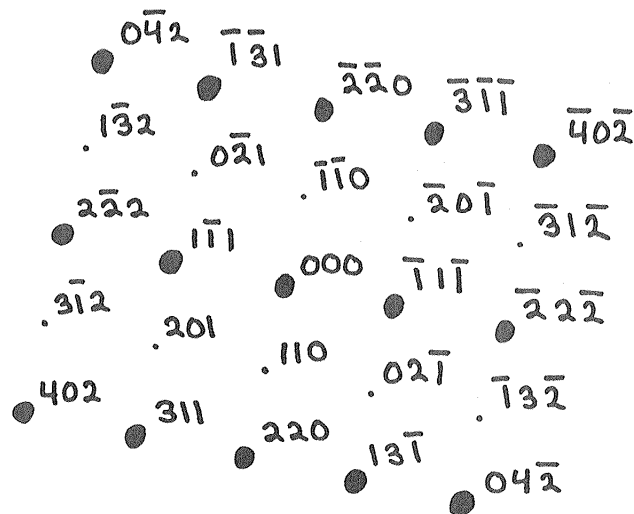
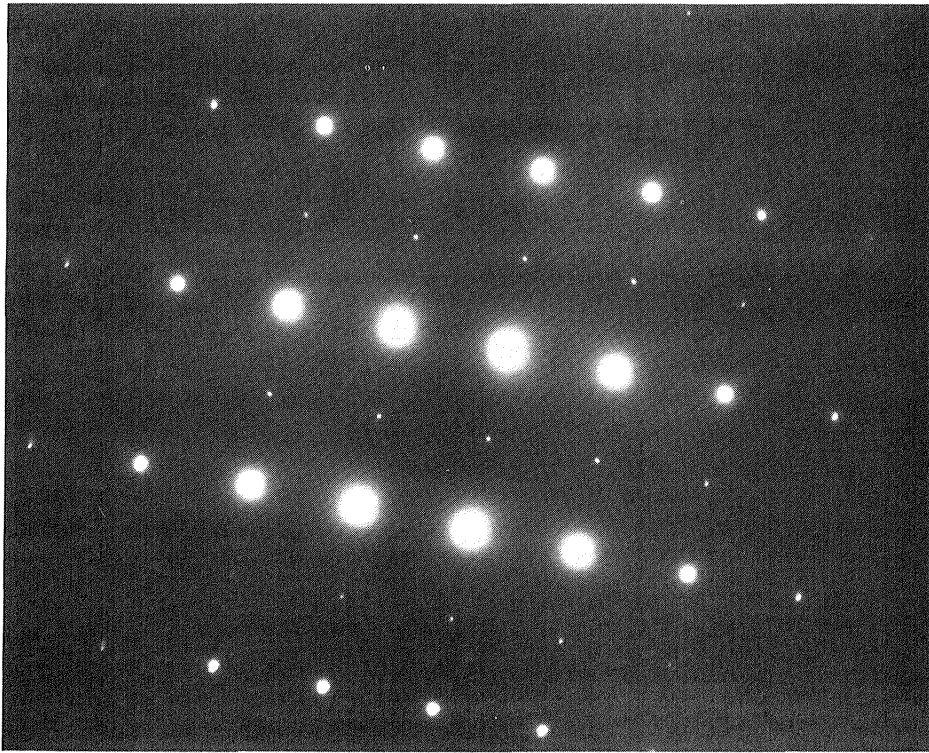


FIGURE 29e: Typical SAD pattern for aged and unaged specimens.
The pattern shown is that of a $[112]$ zone.

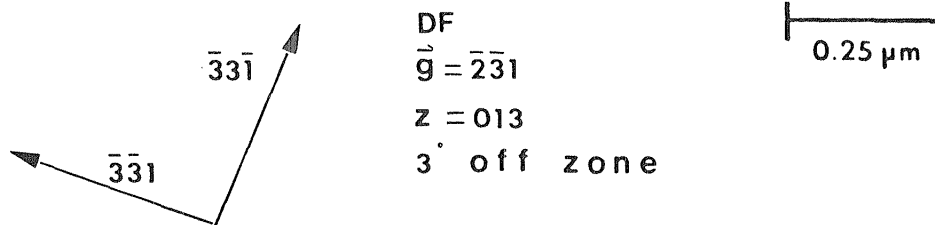
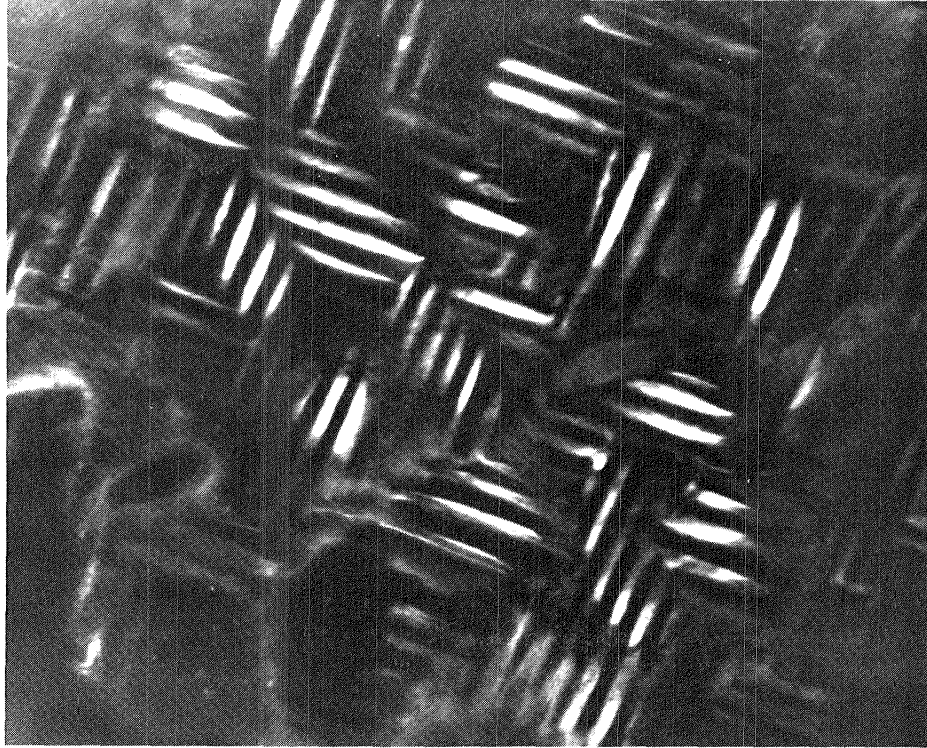


FIGURE 30: A dark-field TEM of an as-received specimen that was aged at 1500°C for 1525 minutes. The precipitates are aligned in two $\langle 3\bar{3}1 \rangle$ directions.

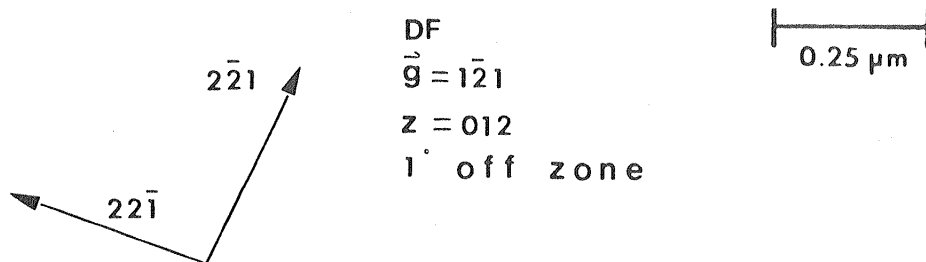


FIGURE 31: A dark-field TEM of an as-received specimen that was aged at 1500°C for 1525 minutes. The precipitates are aligned in two $\langle 2\bar{2}1 \rangle$ directions.

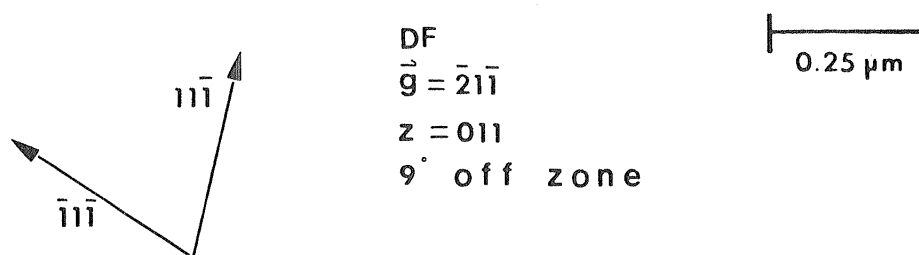
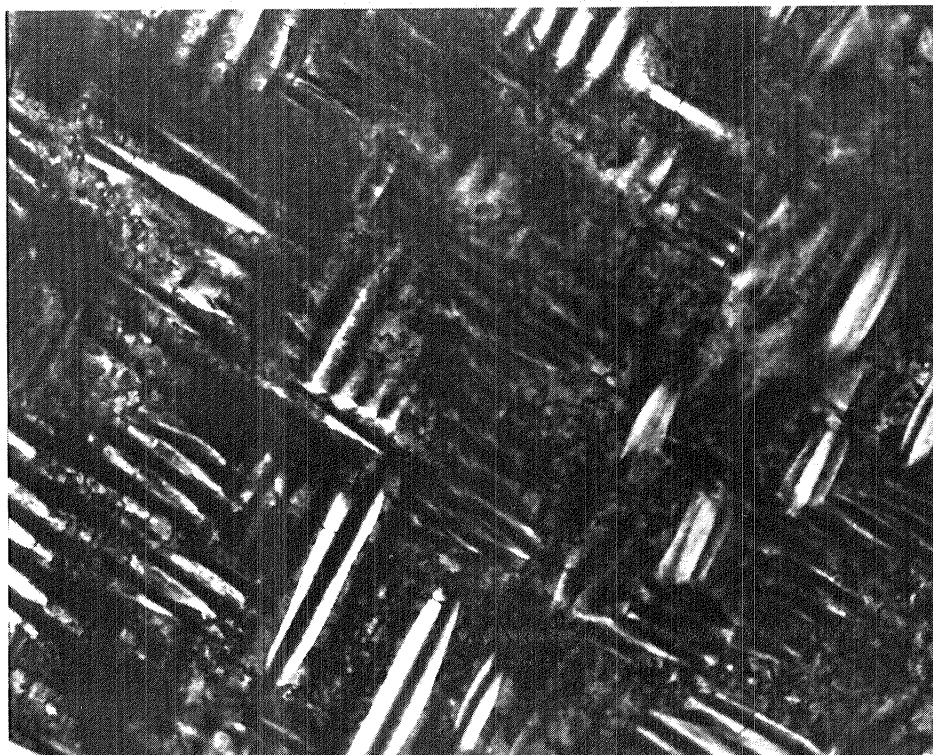
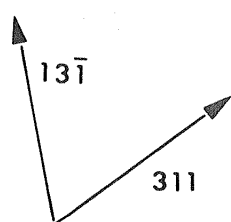
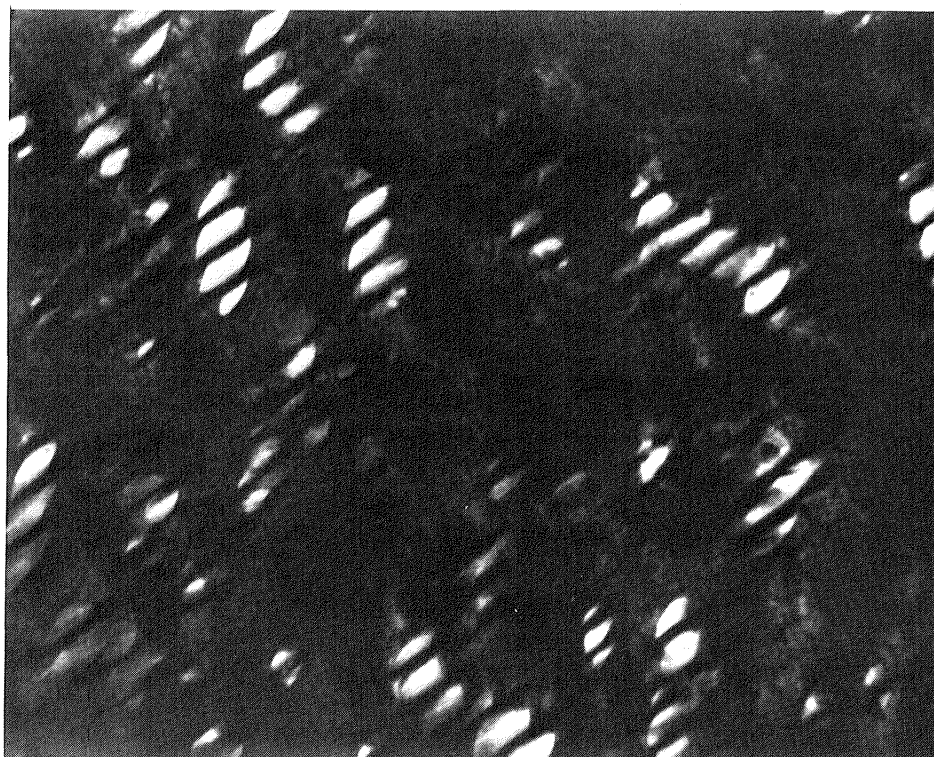


FIGURE 32: A dark-field TEM of an as-received specimen that was aged at 1500°C for 1525 minutes. The precipitates are aligned in two $\langle 111 \rangle$ directions.



DF
 $\vec{g} = 1\bar{3}2$
 $z = \bar{1}12$
 7° off zone

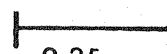
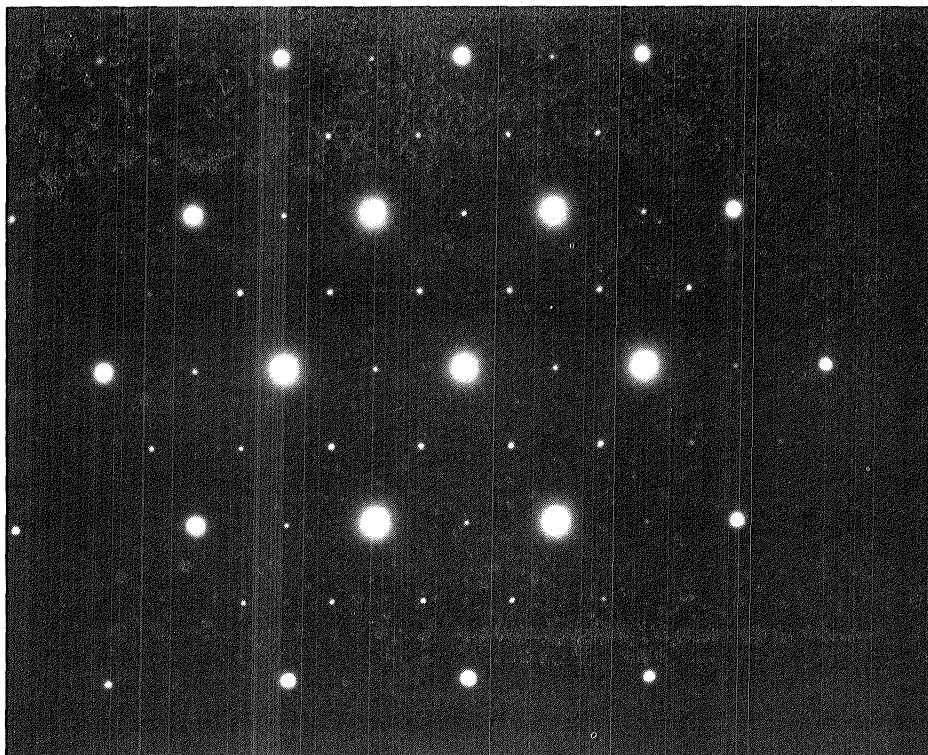
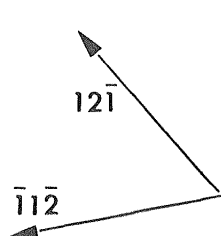
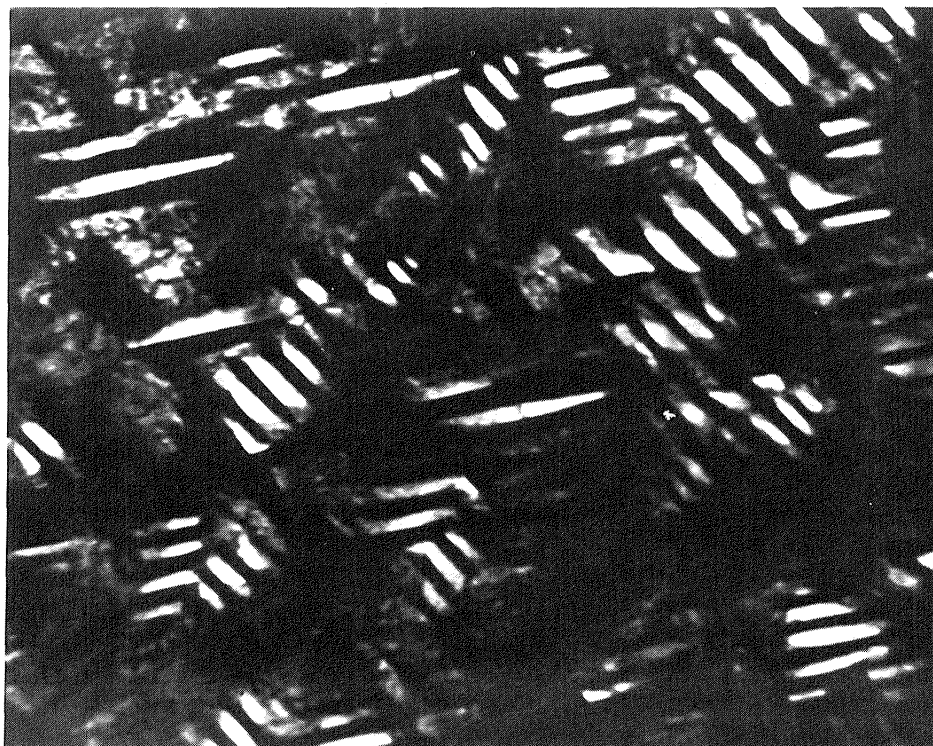

 0.25 μm

FIGURE 33: A dark-field TEM of an as-received specimen that was aged at 1500°C for 1525 minutes. The precipitates are aligned in two $\langle 311 \rangle$ directions.



$\begin{array}{ccccccc}
\cdot \bar{2}\bar{3}1 & \bullet \bar{2}\bar{2}0 & \cdot \bar{2}\bar{1}\bar{1} & \bullet \bar{2}0\bar{2} & \cdot \bar{2}1\bar{3} & & \\
\cdot \bar{1}\bar{2}1 & \cdot \bar{1}\bar{1}0 & \cdot \bar{1}0\bar{1} & \cdot \bar{1}1\bar{2} & & & \\
\bullet 0\bar{2}\bar{2} & \cdot 0\bar{1}1 & \bullet 000 & \cdot 01\bar{1} & \bullet 02\bar{2} & & \\
\cdot 1\bar{1}\bar{2} & \cdot 101 & \cdot 110 & \cdot 12\bar{1} & & & \\
\cdot 2\bar{1}\bar{3} & \bullet 202 & \cdot 211 & \bullet 220 & \cdot 23\bar{1} & &
\end{array}$

FIGURE 34: Typical SAD pattern for aged and unaged specimens. The pattern shown is that of a $[\bar{1}11]$ zone.



DF
 $\vec{g} = \bar{2}\bar{1}\bar{1}$
 $z = \bar{1}11$
 5° off zone

0.25 μm

FIGURE 35a: Dark-field TEM of an as-received PSZ specimen aged 1525 minutes at 1500°C showing a single tetragonal variant that was imaged with a $\{112\}$ spot.

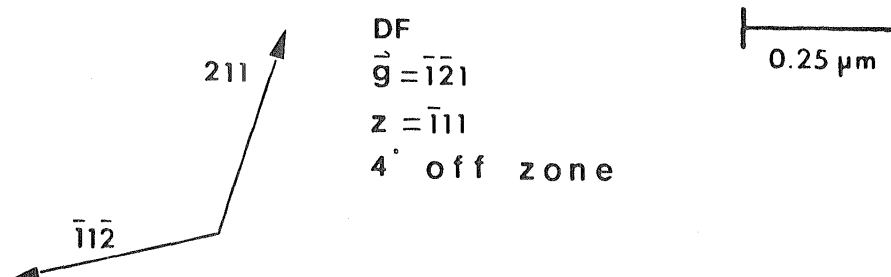
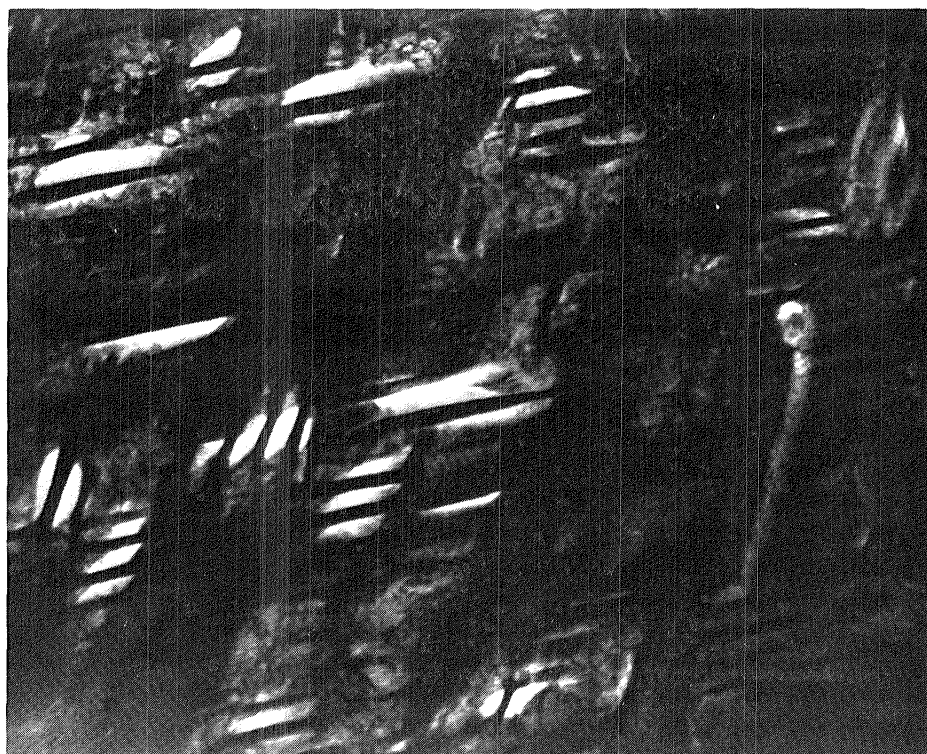
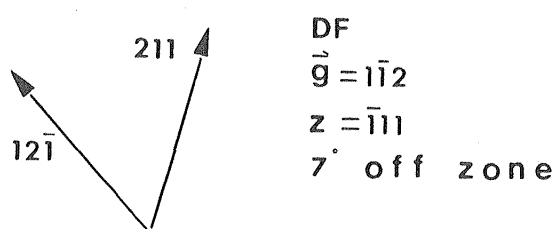
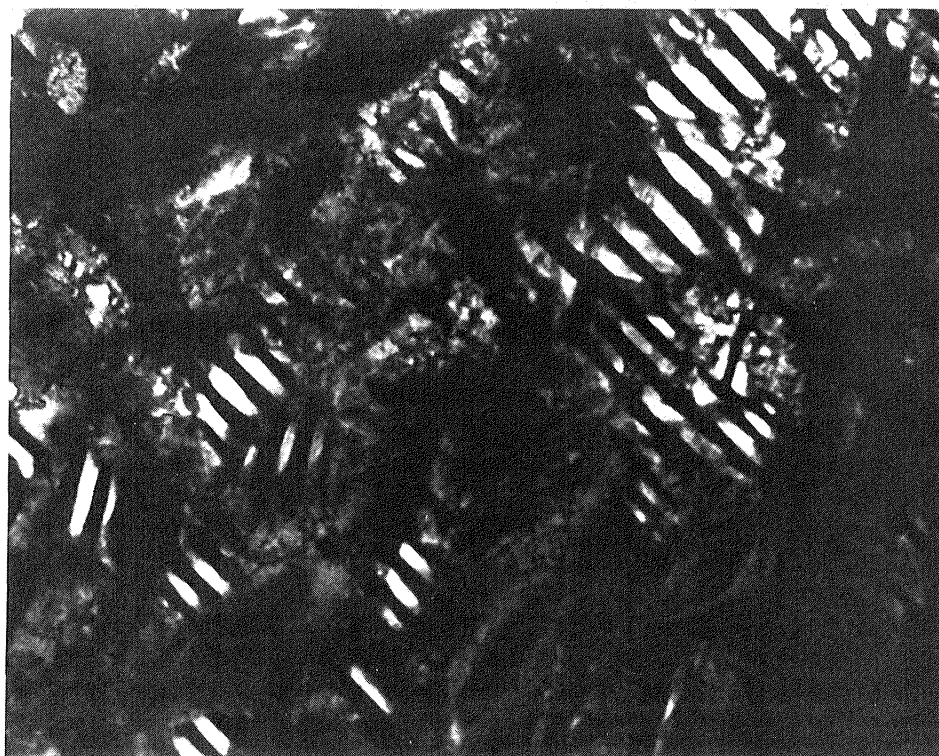


FIGURE 35b: Dark-field TEM of an as-received PSZ specimen aged 1525 minutes at 1500°C , showing a single tetragonal variant that was imaged with a $\{112\}$ spot.



DF
 $\vec{g} = 1\bar{1}2$
 $z = \bar{1}11$
 7° off zone


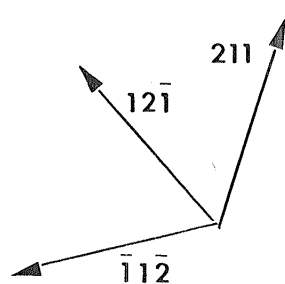
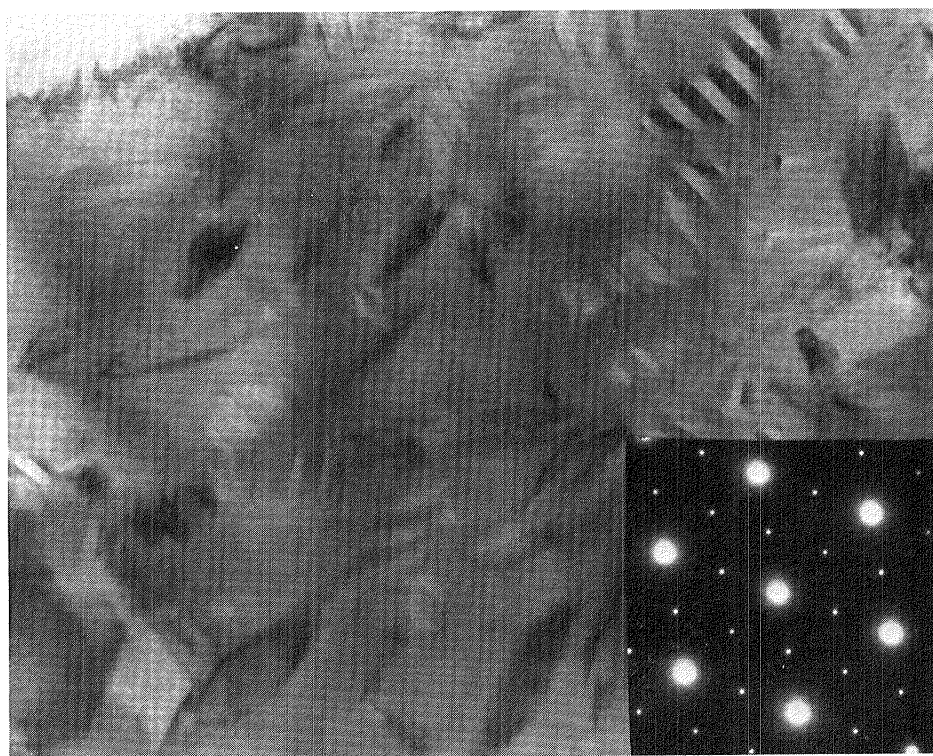

 0.25 μm

FIGURE 35c: Dark-field TEM of an as-received PSZ specimen aged 1525 minutes at 1500°C, showing a single tetragonal variant that was imaged with a $\{112\}$ spot.



BF
multi-beam
 $z = \bar{1}11$
 7° off zone

0.25 μm

FIGURE 35d: Bright-field TEM of the area of an as-received specimen aged 1525 minutes at 1500°C shown in Figures 35a, 35b, and 35c.

PLANES	100	010	001	011	$\bar{0}\bar{1}\bar{1}$	101	$\bar{1}0\bar{1}$	110	$\bar{1}\bar{1}0$
ZONES									
$\bar{1}\bar{1}\bar{1}$	$0\bar{1}\bar{1}$	$\bar{1}0\bar{1}$	110	$0\bar{1}\bar{1}$	[211]	[$\bar{1}2\bar{1}$]	101	[$\bar{1}\bar{1}\bar{2}$]	$\bar{1}\bar{1}0$
$\bar{1}\bar{1}\bar{2}$	$0\bar{2}\bar{1}$	$\bar{2}0\bar{1}$	110	$\bar{1}\bar{1}\bar{1}$	[311]	[$\bar{1}3\bar{1}$]	$\bar{1}\bar{1}\bar{1}$	$\bar{1}\bar{1}\bar{1}$	$\bar{1}\bar{1}0$
013	$0\bar{3}\bar{1}$	$\bar{1}00$	100	$\bar{1}00$	100	$\bar{1}3\bar{1}$	$\bar{1}3\bar{1}$	[$\bar{3}3\bar{1}$]	[$\bar{3}3\bar{1}$]
012	$0\bar{2}\bar{1}$	$\bar{1}00$	100	$\bar{1}00$	100	$\bar{1}2\bar{1}$	$\bar{1}2\bar{1}$	[$\bar{2}2\bar{1}$]	[$\bar{2}2\bar{1}$]
011	$0\bar{1}\bar{1}$	$\bar{1}00$	100	-	100	[$\bar{1}\bar{1}\bar{1}$]	[$\bar{1}\bar{1}\bar{1}$]	$\bar{1}\bar{1}\bar{1}$	$\bar{1}\bar{1}\bar{1}$

FIGURE 36: Table of the directions that correspond to traces of specific planes in specific zones. The directions in brackets, [], correspond to those obtained from the preceding figures (Nos. 30, 31, 32, 33, and 35).

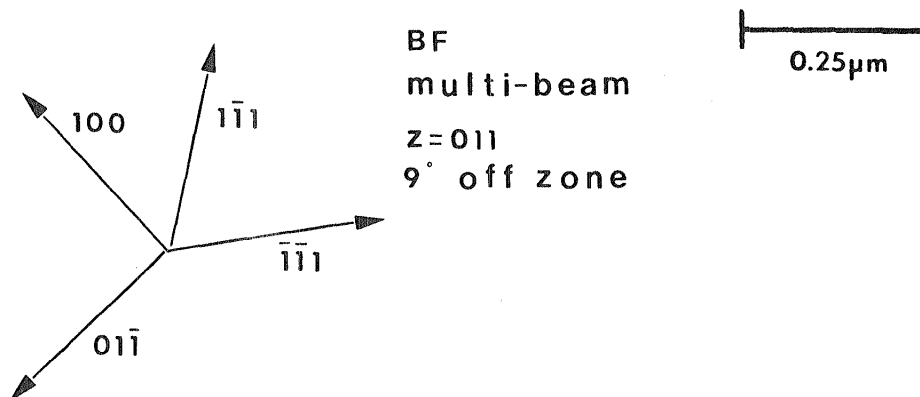
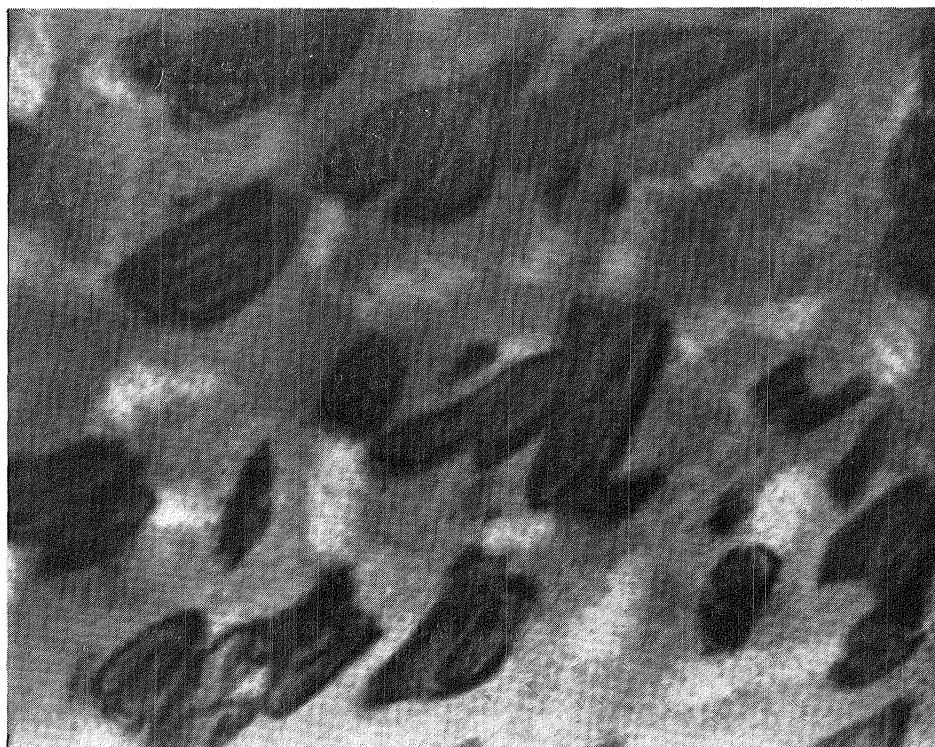


FIGURE 37a: Bright-field TEM of an as-received specimen that was aged for 1525 minutes at 1500°C , showing the true dimensions and/or shapes of the tetragonal precipitates.

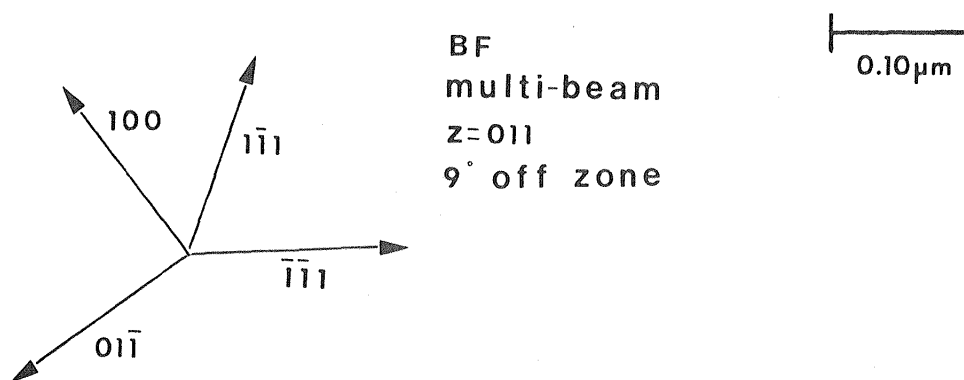
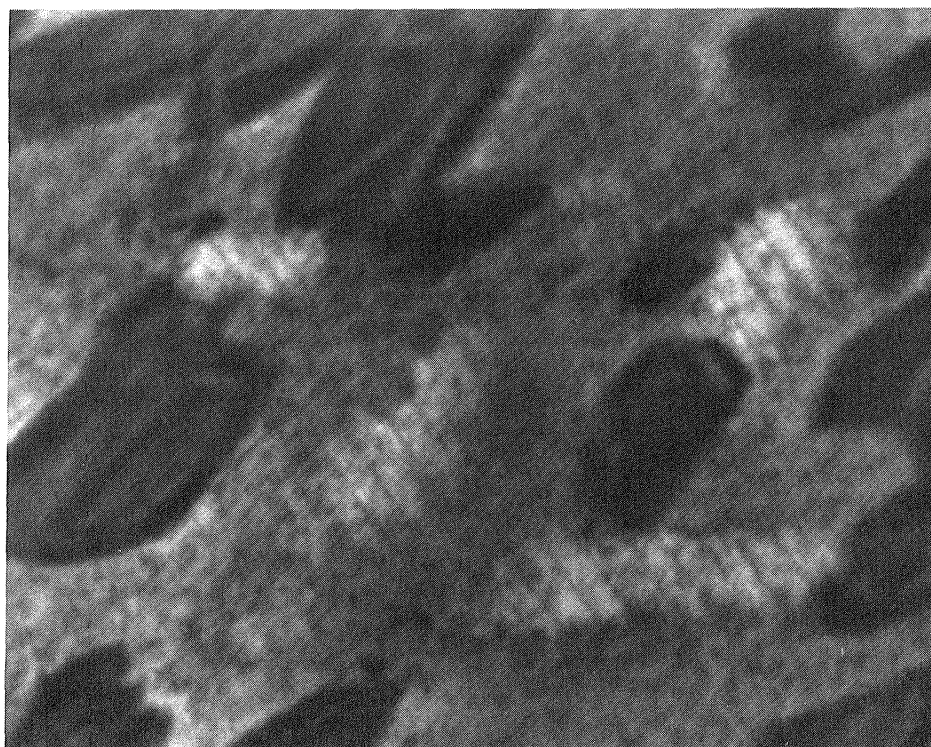


FIGURE 37b: Bright-field TEM of an as-received specimen that was aged for 1525 minutes at 1500°C. This figure is an enlarged view of that in Figure 37a, and shows the dimensions and shapes of the precipitates in more detail.



\nearrow
 $3\bar{1}1$

BF
 $\vec{g} = 3\bar{1}1$

$\overline{\text{---}} \text{---} \overline{\text{---}}$
 0.25 μm

FIGURE 38: A bright-field TEM of a specimen that was solution-annealed-and-quenched and then aged for 10,080 minutes at 1500°C. The rectangular shape of the largest face of the precipitates can readily be observed.

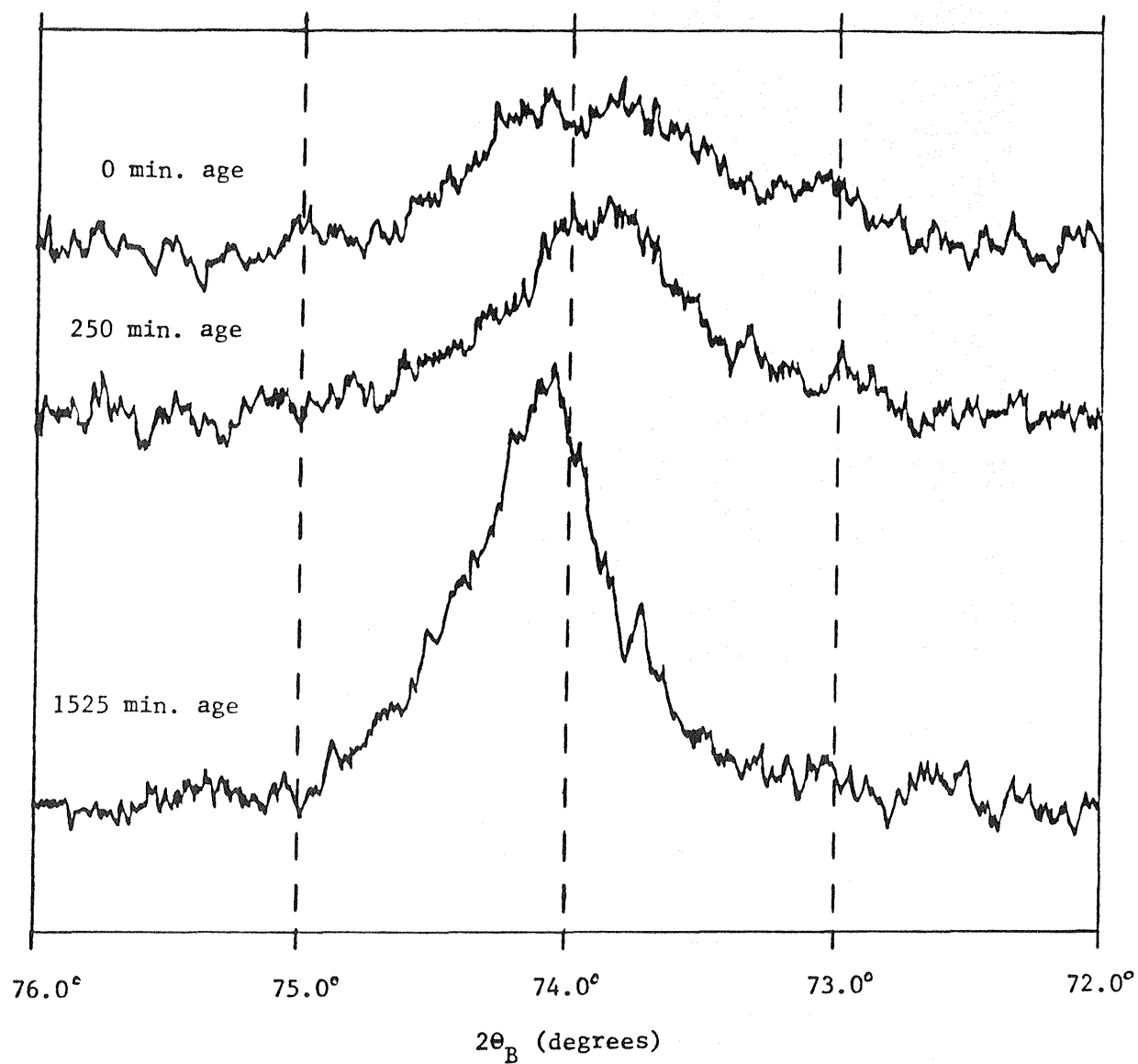


FIGURE 39: Influence of aging the as-received material at 1500°C on diffractometer peak configuration. Note the sharpening of the peaks with increasing aging time.

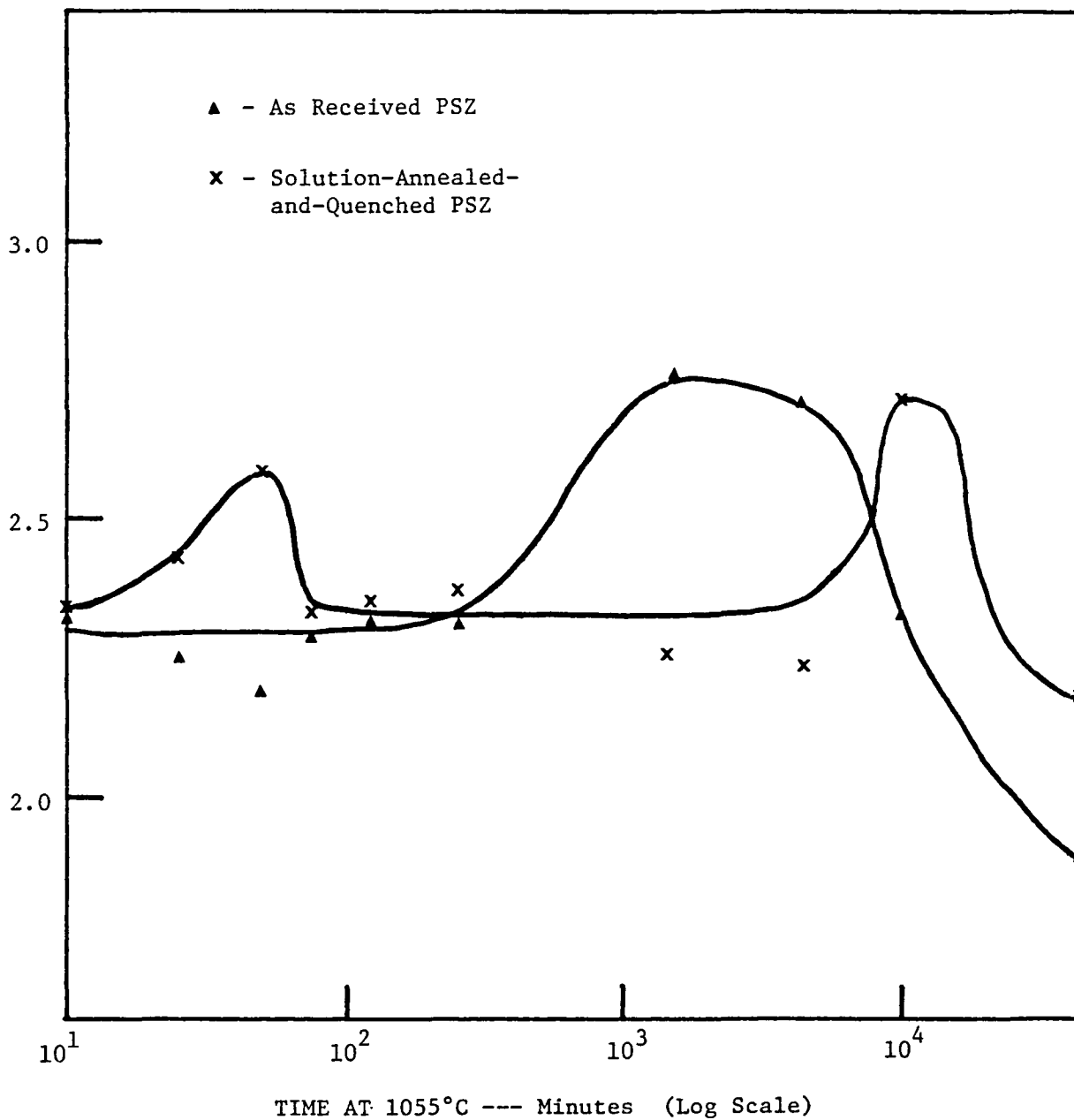


FIGURE 40: Fracture toughnesses of the as-received and the solution-annealed-and-quenched materials as a function of aging time at 1500°C. A Vickers diamond indenter and a 1 Kg load were used for the hardness measurements.

FRACTURE TOUGHNESS OF PSZ

<u>MATERIAL</u>	<u>K_C</u> <u>(MN/M^{3/2})</u>	<u>TRANSFORMATION</u> <u>TOUGHENING</u>	<u>REFERENCE</u>
7.2 Mole-% CaO - ZrO ₂	1.1	No	Green et al. (23)
8.1 Mole-% MgO - ZrO ₂	5.7	Yes	Porter et al. (1)
8.1 Mole-% MgO - ZrO ₂	2	No	Porter et al. (1)
? Mole -% Y ₂ O ₃ - ZrO ₂	6-9	Yes	Gupta et al. (24)
4.5 Mole-% Y ₂ O ₃ - ZrO ₂	2-3	no	Present Study

FIGURE 41: The fracture toughnesses of several partially stabilized zirconias.

1. Report No. NASA CR-165402		2. Government Accession No.		3. Recipient's Catalog No.	
4. Title and Subtitle MICROSTRUCTURE AND MECHANICAL PROPERTIES OF BULK YTTRIA-PARTIALLY-STABILIZED ZIRCONIA				5. Report Date August 1981	
				6. Performing Organization Code	
7. Author(s) Peter G. Valentine, Ralph D. Maier, and Terence E. Mitchell				8. Performing Organization Report No. None	
9. Performing Organization Name and Address Case Western Reserve University Department of Metallurgy and Materials Science Cleveland, Ohio 44106				10. Work Unit No.	
				11. Contract or Grant No. NSG-3252	
12. Sponsoring Agency Name and Address National Aeronautics and Space Administration Washington, D. C. 20546				13. Type of Report and Period Covered Contractor Report	
				14. Sponsoring Agency Code 505-33-12	
15. Supplementary Notes Final report. Project Manager, Michael A. Gedwill, Jr., Materials Division, NASA Lewis Research Center, Cleveland, Ohio 44135. Peter G. Valentine is presently in the U. S. Air Force; Ralph D. Maier is associated with Gould Inc., Cleveland, Ohio; and Terence E. Mitchell is a Professor of Metallurgy and Materials Science at Case Western Reserve University, Cleveland, Ohio.					
16. Abstract A commercially available bulk 4.5 mole percent yttria-(Y ₂ O ₃)-partially-stabilized zirconia (PSZ) was studied by light microscopy, X-ray analysis, microhardness measurement, and fracture toughness testing. The growth of the precipitates and the phase transformations were studied as a function of aging in air at 1500° C. Aging curves were constructed for both the as-received and the solution-annealed-and-quenched materials; the curves showed hardness peaks at 1397 and 1517 kg/mm ² , respectively. A total of twelve different types of tetragonal precipitates were found. The rectangular plate-shaped tetragonal precipitates were found to have a {110} habit plane. Grinding of the Y ₂ O ₃ PSZ into powder did not cause a significant amount of metastable tetragonal precipitates to transform into the monoclinic phase, thus indicating that transformation toughening is not a significant mechanism for the material. The fracture toughness of the aged and of the unaged solution-annealed-and-quenched PSZ was found to be between 2 and 3 MN/m ^{3/2} .					
17. Key Words (Suggested by Author(s)) Ceramics Coatings Thermal barrier				18. Distribution Statement Unclassified - unlimited STAR Category 26	
19. Security Classif. (of this report) Unclassified		20. Security Classif. (of this page) Unclassified		21. No. of Pages 81	
				22. Price*	

End of Document